Cell-projection pumping: A hydrodynamic cell-stiffness dependent mechanism for cytoplasmic transfer between mammalian cells

Hans Zoellner[1,2*], Navid Paknejad[3], James Cornwell[1], Belal Chami[1], Yevgeniy Romin[3], Vitaly Boykov[3], Sho Fujisawa[3], Elizabeth Kelly[1], Garry W. Lynch[4], Glynn Rogers[1], Katia Manova[3], Malcolm A.S. Moore[2]

[1] The Cellular and Molecular Pathology Research Unit, Oral Pathology and Oral Medicine, Faculty of Medicine and Health, The University of Sydney, Westmead Hospital, Westmead, NSW 2145, Australia

[2] Cell Biology, The Memorial Sloan Kettering Cancer Center, 430 E 67th St, RRL 717, New York, NY

[3] Molecular Cytology, The Memorial Sloan Kettering Cancer Center, 415-417 E 68 Street, ZRC 1962, New York, NY

[4] Sydney Medical School, Faculty of Medicine and Health, and Sydney School of Veterinary Science, Faculty of Science, The University of Sydney, The University of Sydney, NSW, 2006, Australia

Corresponding Author: H Zoellner
The Cellular and Molecular Pathology Research Unit, Oral Pathology and Oral Medicine, Faculty of Medicine and Health Sciences, The University of Sydney, Westmead Hospital, Westmead, NSW 2145, Australia
Email: hans.zoellner@sydney.edu.au
Ph: +61 2 8890 7892,
FAX: +61 2 9893 8671

Abstract
We earlier reported cytoplasmic fluorescence exchange between cultured human fibroblasts and malignant cells (MC). Current time-lapse microscopy showed most exchange was from fibroblasts into MC, with less in the reverse direction. Surprisingly, transfer was not via tunneling nanotubes, but by often branching cell-projections instead, and transfer events coincided with retraction of donor cell-projections. Increased hydrodynamic pressure in retracting cell-projections, normally returns cytoplasm to the cell body. We hypothesize 'cell-projection pumping' (CPP), where cytoplasm in retracting cell-projections equilibrates partially into adjacent recipient cells via temporary inter-cellular cytoplasmic continuities. Plausibility for CPP was explored via a mathematical model, which predicted preferential CPP into cells with lower cell stiffness, since pressure equilibrates towards least resistance. Predictions from the model were satisfied when fibroblasts were co-cultured with MC, and fluorescence exchange related with cell stiffness measured by atomic force microscopy. When transfer into 5000 simulated recipient MC or fibroblasts was studied in computer simulations, inputting experimental cell stiffness and donor cell fluorescence values, generated transfers to simulated recipient cells similar to those seen by experiment, including the expected inverse relationship between receptor cell stiffness and fluorescence uptake. We propose CPP as a novel mechanism in mammalian inter-cellular cytoplasmic transfer and communication.

Introduction
We earlier described the exchange of fluorescently labeled membrane and cytoplasmic protein, as well as alkaline phosphatase between cultured human fibroblasts and malignant cells (MC) [1], and others have made similar observations [2-13]. Notably, we found altered phenotype subsequent to inter-cellular transfer, and recognize implications for cancer biology, inflammation, wound healing and development [1,14,15].

Cytoplasmic transfer modulating phenotype is described as being via plasmodesmata in plants, septal pores in fungi, and tunnelling nanotubes (TNT) in mammalian cells [12,16,17]. Further, there are numerous reports of mitochondrial exchange between mammalian cells by a still uncertain mechanism, and this too can affect cell phenotype [5-10,18].

TNT are long straight tube-like connections that establish cytoplasmic continuity between individual cells, and are known to mediate exchange of cytoplasm and organelles. When seen in cell culture, TNT are typically suspended above the culture substrate, and have the appearance of taught wire-like connections [11-13,16,19-23]. Interestingly, TNT-mediated organelle transfer occurs via active ATP dependent mechanisms [11-13]. Although other cell-projections are not considered capable of similar transfer [24], short-straight TNT-like structures mediating exchange have been described as microtubules [2]. In addition to inter-cellular cytoplasmic exchange via TNT, exosomes and other micro-vesicular structures can mediate the transfer of material from one cell to another, and this can affect cell phenotype [19,25], but as will be seen below, neither TNT or exosomes contributed significantly to inter-cellular cytoplasmic exchange in our experiments.

Here we describe confocal laser scanning microscopy (CLSM) studies, initiated to address the possibility that TNT were responsible for the intercellular exchange process we previously reported [1]. Consistent with our earlier work, exchange was primarily from fibroblasts to MC, but surprisingly, time-lapse

microscopy excluded a role for TNT and revealed instead that exchange occurred during apparently spasmodic retraction of donor cell-projections, while the extent of overall transfer was often remarkable (Fig. 1a). Please note necessity to use permanent labels, such as the fluorescent lipophilic markers DiD and DiO in the current study, to demonstrate total cytoplasmic transfer, because such labels persist long after degradation of the originally labelled structures. By contrast, cell turn-over renders highly specific organellar or protein labels unreliable for detecting cumulative cytoplasmic transfer between cells.

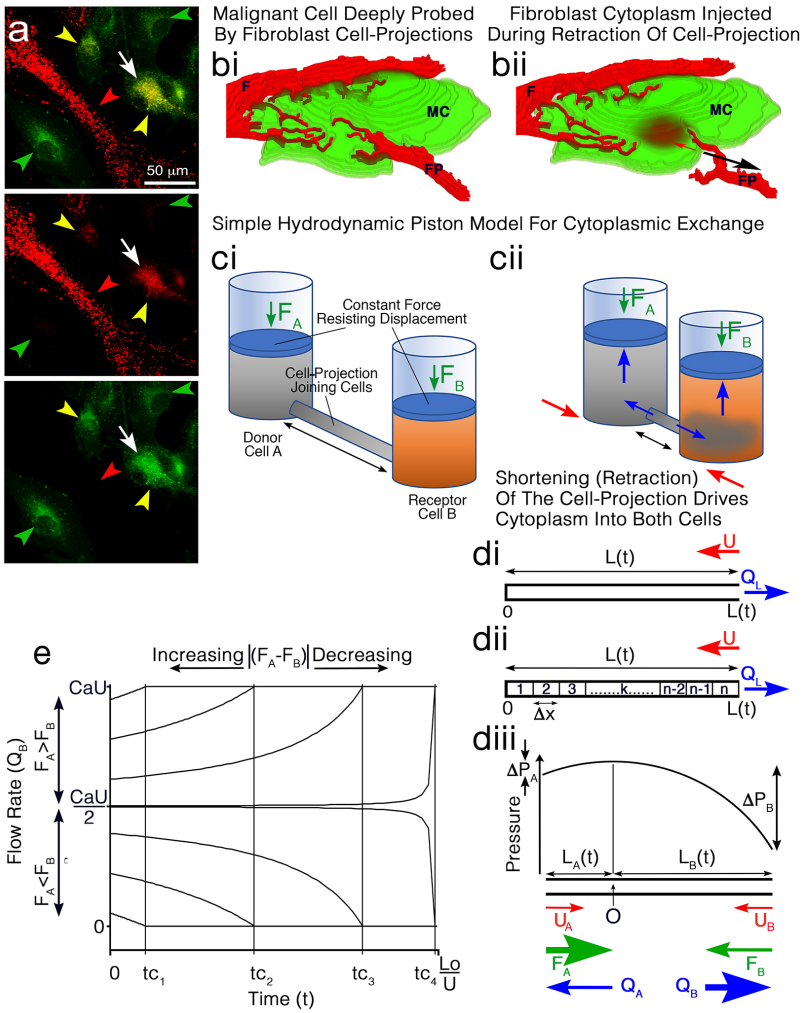

Figure 1. *The cell-projection pumping (CPP) hypothesis for transfer of cytoplasmic label.* ***(a)*** *The extent of red fibroblast label transfer to MC was often remarkable and most apparent when red and green channels were seen separately. While some MC had no fibroblast-red label (green arrow heads), fibroblast marker was in many MC (yellow arrow heads), occasionally to an extreme extent (white arrows).* ***(bi)*** *The cartoon is drawn from a confocal image containing a MC deeply grooved by fibroblast (F) cell-projections (FP).* ***(bii)*** *If there is a transient inter-cellular cytoplasmic continuity, retraction of the cell-projection (black arrow) drives some fibroblast cytoplasm into the MC (red arrow).* ***(ci)*** *This is modelled with piston-cylinders connected by a cylindrical tube (black arrow) containing a Newtonian fluid from the 'Donor Cell'.* ***(cii)*** *Shortening of the tube (red arrows) mimics cell-projection retraction, driving Donor Cell contents into both 'Donor' and 'Receptor Cells', against constant forces of resistance proportionate to cell stiffness.* ***(di)*** *Consider a close-ended tube with length L(t) contracting at constant rate U (red arrow), and generating a flow rate of a fluid within the tube of Q_L (blue arrow).* ***(dii)*** *Dividing the tube into n cylinders of Δx length, with Δx approaching zero, relates L(t) to pressure and Q_L.* ***(diii)*** *Two such tubes of lengths $L_A(t)$ and $L_B(t)$ are opened and joined at their origins (O), contracting at U_A and U_B ($U_A+U_B=U$) (red arrows), with flow (Q_A and Q_B, blue arrows) against constant forces (F_A and F_B, green arrows) due to and proportionate to cell stiffness (S_A and S_B), such that F=ZS where Z is a constant. Pressure is maximal at Po, and equals F_A and F_B at the open ends, establishing ΔP_A and ΔP_B. Where $F_A>F_B$ ($S_A>S_B$), $L_A(t)<L_B(t)$ and $Q_A<Q_B$; this reverses when $F_A<F_B$ ($S_A<S_B$); while when $F_A=F_B$ ($S_A=S_B$), $Q_A=Q_B$.* ***(e)*** *Q_B is plotted over time for retraction to extinction of a cell-projection. Notably, when $F_A>F_B$ ($S_A>S_B$), there is a time (tc) when $L_A=0$, $Q_A=0$, and remaining flow is Q_B=CaU, where Ca= tube cross-sectional area. When $F_A<F_B$ ($S_A<S_B$), $L_B=0$ at tc, so that $Q_B=0$, and remaining flow is Q_A. Decreasing F_A-F_B (S_A-S_B) increases tc.*

The transferring cell-projections could not be resolved to a high degree of accuracy, because of their rapid movement, paucity of fluorescent labelling, and limitations of CLSM. Nonetheless, they could be visualized with reasonable confidence by occasional fluorescently labelled fibroblast organelles, often in delicate indenting grooves formed by donor fibroblast cell-projections on the surfaces of recipient MC. The manner in which fibroblast cell-projections grooved and indented MC, was consistent with the appreciably greater cell surface stiffness of fibroblasts compared with MC [26].

These observations led us to hypothesize that transfer is by a hydrodynamic pumping mechanism, where retraction of a donor cell-projection raises local cytoplasmic pressure within the cell-projection, and there is coincident transient cytoplasmic continuity between the donor cell-projection and a neighboring receptor cell. This pumps cytoplasm from the donor cell-projection into the recipient cell, while the relative difference in cell stiffness between donor and recipient cells affects the amount of label transferred; a process for which we propose the term 'cell-projection pumping' (CPP) (Fig. 1b).

The hydrodynamic mechanism we propose for CPP through equilibration of local pressure differentials by cytoplasmic flow is in some ways similar to that described in formation of lamellifilopodia [27], blebbing [28,29], and the formation of lobopodia [30].

The current paper explores plausibility of the CPP hypothesis by: a) developing a mathematical model for CPP (Fig. 1c,d,e); b) determining if predictions from the model that correlate cell stiffness with fluorescence, are seen by experiment; and c) using experimental data on cell stiffness and fluorescence exchange to construct computer simulated populations of cells, and determining if simulation results similar to experimental observations can be achieved making biologically reasonable assumptions for variables in the mathematical model.

Results

Time-lapse CLSM indicated exchange of cytoplasmic organelles between cells was via cell-projections with the appearance of branching filopodia and lamelifilopodia. Obvious acquisition of DiD (red) labelled fibroblast organelles was observed in 11 out of 106 DiO (green) pre-labelled MC, during 8 h 15 min co-culture, and 7 out of 71 GFP (green) pre-labelled MC during 25 h co-culture. From this, a total of 18 MC were observed receiving fibroblast organelles, studying 33 h 15 min of time-lapse recordings (Supplementary movies S1-S3; Figs. 2a, 3a,b). Only a single occasion was observed, where DiO (green) labelled organelles were transferred from a single MC to a fibroblast, via broad cell-projection structures with the appearance of laemlifilopodia (Supplementary movie S4). Although occasional large prominent fibroblast organelles were accepted by MC (Supplementary movie S1 Movie; Fig. 2a), most exchange was of smaller organelles, and this was most readily seen when MC were labeled with DiO (green) (Supplementary movie S3, Fig. 3). Note that organellar labelling was used for time-lapse microscopy, because punctate organellar fluorescence is advantageous for tracking the movement of otherwise diffuse cytoplasm.

Because fibroblast cell-projections transferring organelles to MC were largely transparent by CLSM, they could not be resolved to a high degree of accuracy. However, the shape and location of these transparent fibroblast cell-projections could be inferred by careful examination of CLSM z-stack images in time-lapse movies,

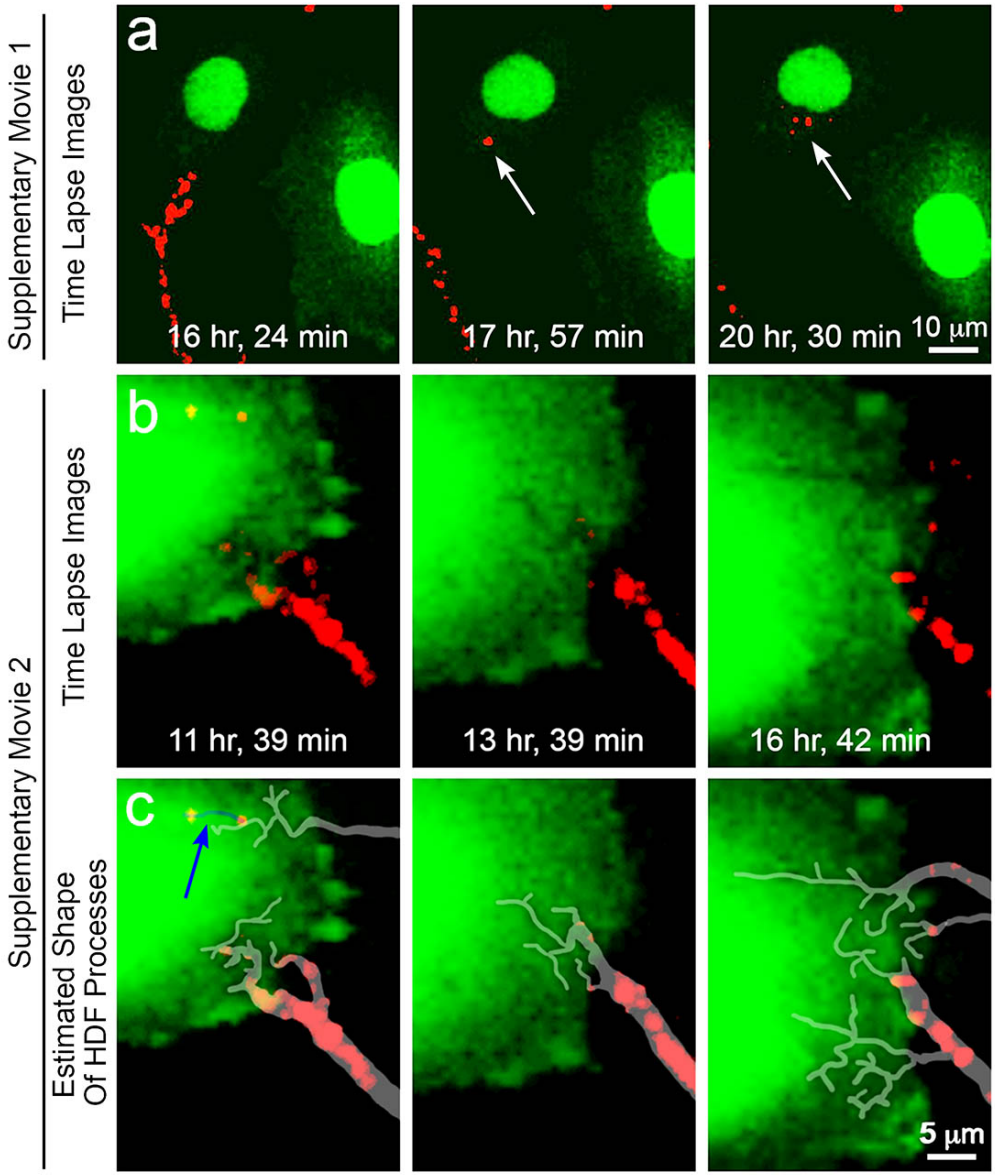

Figure 2. *Frames from Supplementary Movies S1 and S2, showing confocal microscopy time-lapse images of fibroblasts (pre-labelled red with DiD) co-cultured with MM200-B12 melanoma cells (expressing green GFP label).* ***(a)*** *Bright red labelled organelles marked a fibroblast cell-projection that deposited a single large organelle into a green-labelled MM200-B12 cell (white arrow, 17hr, 57min). Fragmentation of organellar label was seen by 20 h 30min.* ***(b)*** *Repeated probing of a MM200-B12 by branching fibroblast cell-projections occurred over time. The location of fibroblast cell-projections was revealed by dark grooves made in the less stiff MM200-B12, as well as by occasional red-labelled organelles, and are marked with white transparency in* ***(c)*** *for clarity. One cell projection containing two red-labelled organelles appeared to spear into the malignant cell (blue transparency and arrow).*

where deep grooves were seen in the surfaces of MC (Figs. 2b,c; 3c,d). We interpret these grooves as having been formed by fibroblast cell-projections with high stiffness, compared with the MC they deeply indented. Confirming our interpretation for the location of these transparent fibroblast cell-projections, was the presence of occasional scattered DiD labeled fibroblast organelles within the grooves (Fig, 2b,c; Fig. 3c,d; Supplementary movies S2 and S3).

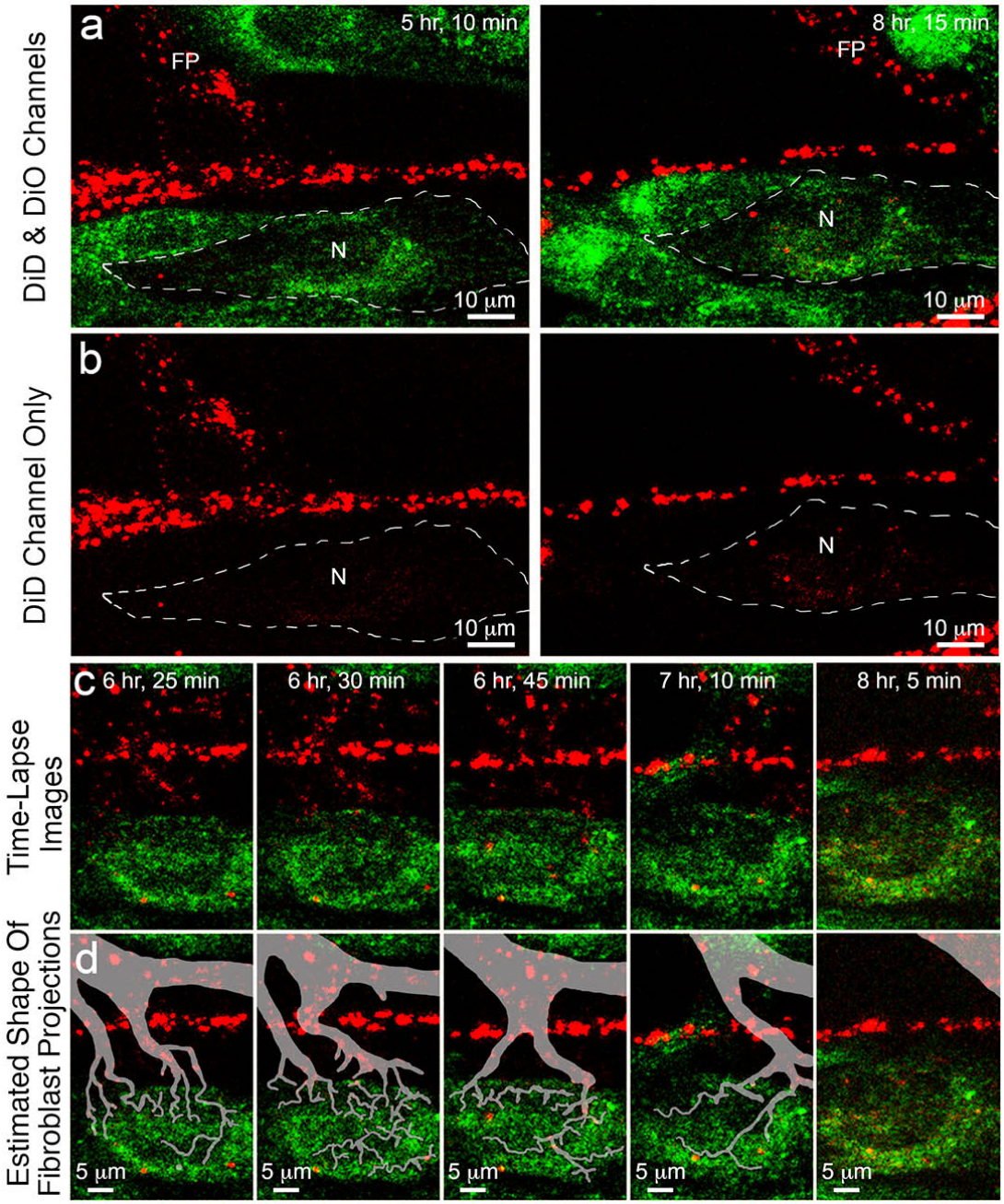

Figure 3. *Frames from Supplementary Movie S3, showing confocal microscopy time-lapse images of fibroblasts (pre-labelled with DiD-red) co-cultured with MM200-B12 melanoma cells (pre-labelled with DiO-green).* ***(a, b)*** *A MM200-B12 (white dashed outline) received appreciable red fibroblast organellar labelling between 5 h 10min and 8 h 15min, most clearly seen when the green channel is excluded (b).* ***(c)*** *This was from a broad fibroblast cell-projection (FP) that swept past the melanoma cell, indenting and grooving the recipient cell with numerous smaller branching cell-projections, no longer seen by 8 h 5min.* ***(d)*** *White transparency marks the location of fibroblast cell-projections grooving the melanoma cell.*

Fibroblast cell-projections indenting MC, appeared as tree-like branching networks that terminated in long filopodia-like extensions (Supplementary movies S2 and S3; Figs. 2b,c, 3c,d). While the overall shape of fibroblast cell-projections was stable over time, the fine terminal branches were labile in shape and varied within the 3 and 5 min intervals between time-lapse frames (Supplementary movies S2 and S3; Figs. 2b,c; 3c,d). Supporting our interpretation for the presence of fibroblast cell-

projections in MC grooves, was that the MC grooves ceased to be apparent when large fibroblast cell-projections became sufficiently distant, as seen comparing Fig. 3c recorded at 7 h 10 min, with Fig. 3c recorded at 8 h 5 min.

Cell-projections alternately probed and retracted from individual receptor cells, and episodes of organellar transfer appeared to coincide with retraction events (Supplementary movies S1-S4).

Occasional TNT were observed, but observations excluded a significant role in the observed transfers for TNT, as well as for phagocytosis of cell fragments, exosomes, or passive label diffusion (Figs. 1a, 2, 3; Supplementary Figs. S1,S2,S3; Supplementary movies S1-S4). It was evident from time-lapse movies, that organellar transfer from donor to recipient cells could only occur if there were transient cytoplasmic continuities through fused plasma membrane windows between the two cell types, similar to that established for TNT, but in this instance occurring via cell-projections, often in the size range of filopodia.

Lacking high resolution images of the cell-projections through which transfer occurred, but having nonetheless observed that these structures transferred cytoplasmic organelles during episodes of cell-projection retraction, we sought to explain our observations on basis of our CPP hypothesis as outlined above (Fig. 1b,c).

Mathematical model for CPP. Detailed development of the mathematical model is provided below in the materials and methods. In brief, cytoplasm is assumed to behave as a Newtonian fluid, and Pascal's Law is interpreted as rendering the results of modelling independent of geometric factors other than the radius and length of the cell-projection [31]. The Hagen-Poiseuille equation for laminar flow of a Newtonian fluid in a tube [32], is incorporated in expressions describing a simple two-chamber system (Fig. 1c). Relationships between pressure and fluid flow are first considered for a tube with a single closed end, in which contraction at a constant rate drives fluid flow out of the open end (Fig. 1di, dii). Two such tubes are then considered, with previously closed ends now joined and opened to establish continuity, and opening into two separate cells. Flow from both open ends is opposed by constant forces proportionate to the stiffness of the two cells joined, establishing a point at the origins of the two original tubes where pressure is maximal and there is no flow (Fig. 1diii). Differing stiffness between cells results in differing pressure and flow. It should be noted that although Young's modulus is the accepted measure for cell stiffness, the cell cannot be assumed to behave as a Hookean spring, and the current model assumes stiffness exerts a constant resistance against changing internal pressure

Expressing this argument mathematically results in equation (1), where: Q_B is the flow rate into Receptor Cell B; S_A and S_B are the stiffness values for Donor Cell A and Receptor Cell B respectively; Z is a constant cell stiffness correction factor; ρ is the resistance per unit length of the cell-projection; L_0 is the length of the cell-projection at time 0; U is the rate of retraction; t is time; and Ca is the cross-sectional area of the cell projection.

$$Q_B = \frac{Z\cdot(S_A - S_B)}{\rho\cdot(L_0 - U\cdot t)} + \frac{Ca\cdot U}{2} \qquad (1)$$

This equation is represented graphically in Fig. 1e, illustrating Q_B from t=0 to the time at which retraction extinguishes a cell-projection, for pairings of Donor and Receptor Cells A and B with differing stiffness values. Integration of these curves determines total volume transfers by CPP.

The mathematical model predicts preferential flow towards cells with lower stiffness. Further, given variability in cell stiffness within each population of co-cultured cells A and B, receptor cell-stiffness and the volume of cytoplasm acquired by CPP should be inversely related.

Experimental measurement of cell stiffness and fluorescence in co-cultured cells satisfied predictions of the mathematical model. Fluorescence microscopy of a co-culture of fibroblasts with SAOS-2, revealed the most evident transfer of fluorescent label was from fibroblasts to SAOS-2, with less clear fluorescence transfer from SAOS-2 to fibroblasts. Fluorescence and atomic force microscopy (AFM) stiffness data for these cells are shown in Fig. 4. Although micro-domains varied greatly in stiffness across the surfaces of individual cells, stiffness fingerprints clearly demonstrated that fibroblasts were stiffer and had lower cell height compared with SAOS-2 (Mann Whitney U Test, $p < 0.0001$).

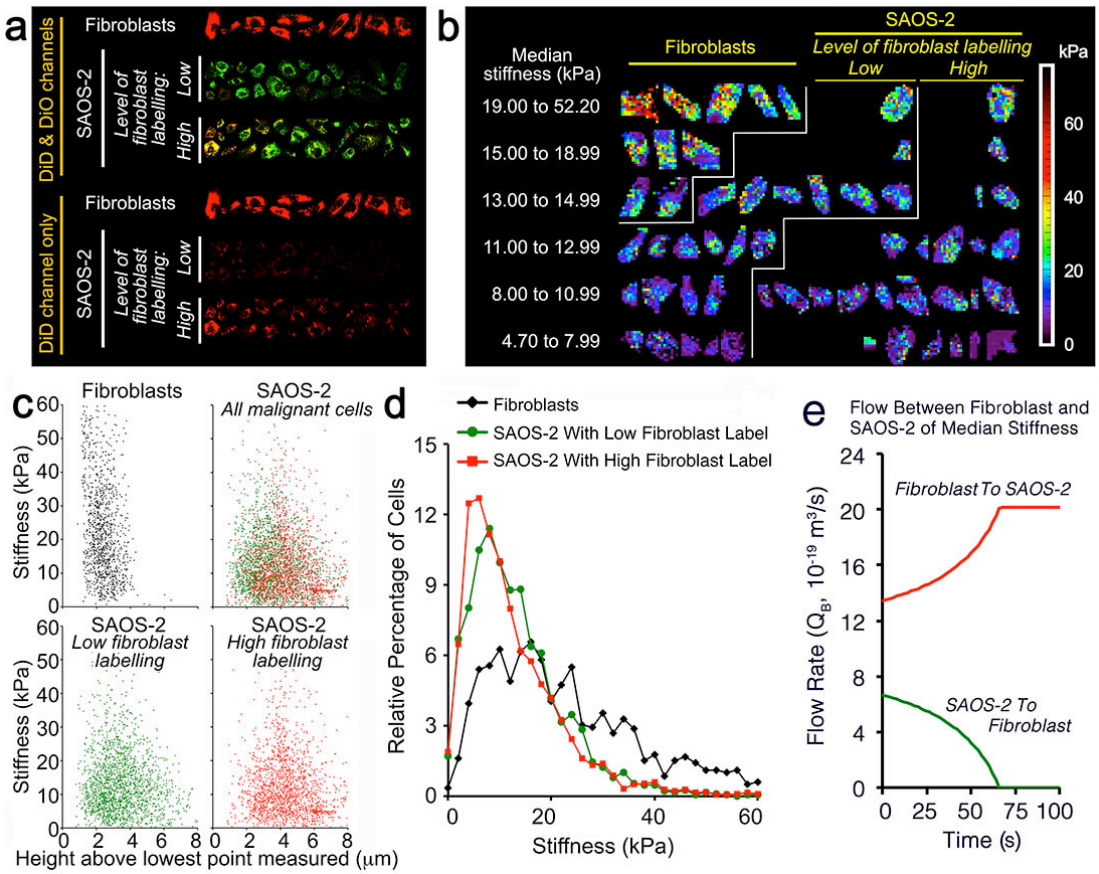

Figure 4. *The relationship between cell stiffness and height in SAOS-2 (pre-labelled with DiO-green) co-cultured for 24 h with fibroblasts (pre-labelled with DiD-red), and mathematical modelling of CPP between cells of median stiffness.* ***(a)*** *DiD (red) levels were quantitated to identify fibroblasts, SAOS-2 with high fibroblast label, and SAOS-2 with low fibroblast label.* ***(b)*** *Although it was not possible to scan the entirety of all cells shown in 'a' by AFM, median values of stiffness scans indicated fibroblasts were stiffer than SAOS-2, and that SAOS-2 with high fibroblast label were usually less stiff than SAOS-2 with low fibroblast label.* ***(c)*** *This was supported in stiffness fingerprints, demonstrating that fibroblasts (black dots) had greater stiffness and lower cell height compared to SAOS-2 (red and green dots) (Mann Whitney U Test, $p < 0.0001$). Further, stiffness values for SAOS-2 with low fibroblast labeling (green dots) were higher than for SAOS-2 with high fibroblast labelling (red dots), while the reverse was the case with regard to height measurements (Mann Whitney U Test, $p < 0.0004$).* ***(d)*** *Relative percentage distribution plots binned at 2 kPa for stiffness.* ***(e)*** *CPP was modelled between a fibroblast and SAOS-2, each of median cell stiffness, and examining exchange from fibroblast to SAOS-2 (red), as well as from SAOS-2 to fibroblast (green). Results were consistent with the CPP hypothesis.*

Label transfer varied in extent amongst SAOS-2, with some SAOS-2 having very high and others negligible fibroblast labeling (Fig. 4a). As predicted, SAOS-2 with high fibroblast labeling had lower stiffness compared with SAOS-2 with low fibroblast labeling (Mann Whitney U Test, $p < 0.0004$) (Fig. 4b,c,d). In addition, higher uptake of fluorescence by CPP correlated with greater cell height (Mann Whitney U Test, $p < 0.0004$).

Fig 4e shows CPP flow rates for transfer from a fibroblast to a SAOS-2, as well as from a SAOS-2 to a fibroblast, assigning median cell stiffness for fibroblasts (18,765 Pa) and SAOS-2 (11,181 Pa), and biologically reasonable assumptions for: cell-projection retraction rate (1×10^{-6}m/s), viscosity (2.5×10^{-3} Pa.s), length at time zero (100 μm), and radius (0.8 μm) of the cell-projection. Significant flow was predicted by the mathematical model in these conditions.

Satisfying a further prediction for the CPP model, was that similar to observations in SAOS-2, uptake of fluorescence from SAOS-2 by fibroblasts was negatively correlated with fibroblast cell stiffness, while there was also a positive correlation with cell height (Mann Whitney U Test, $p < 0.0001$) (Fig. 5). Experimental results thus satisfied all predictions from the mathematical model.

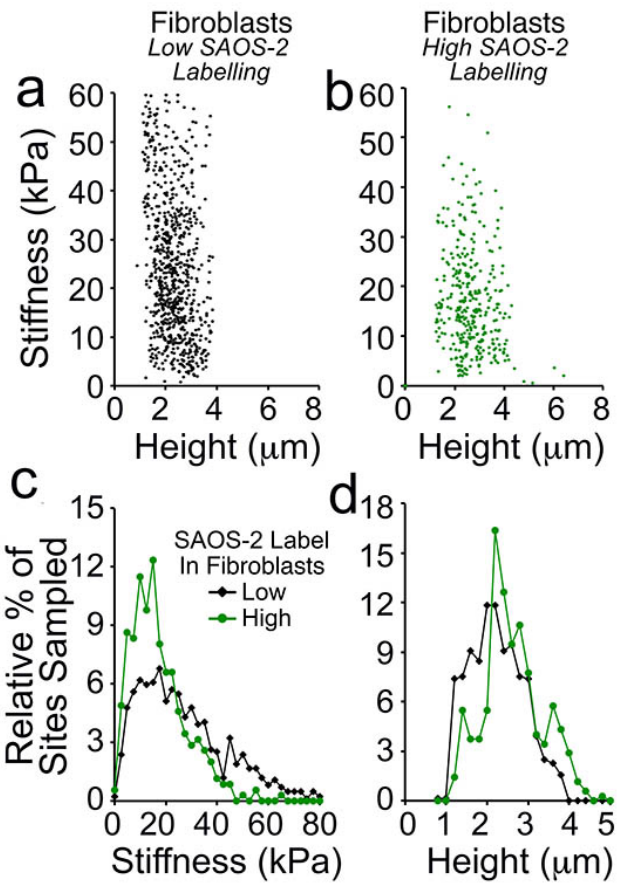

Figure 5. *Stiffness fingerprints and proportional distribution plots comparing stiffness and height AFM measurements for fibroblasts in co-culture with DiO pre-labelled SAOS-2, dependent on whether fibroblasts had high or low levels of SAOS-2 labelling.* ***(a,b)*** *Stiffness fingerprints revealed that fibroblasts with low SAOS-2 labelling had generally higher stiffness and lower cell height measurements (a), compared with fibroblasts with high SAOS-2 labelling (b) (Mann Whitney U Test, $p < 0.0001$).* ***(c,d)*** *Proportional distribution plots binned at 2.5 kPa for stiffness and 0.2 μm for height measurements, further confirmed the visual impressions from stiffness fingerprints.*

Results of numerical MATLAB simulations agreed with experimental observations and satisfied predictions from the mathematical model. Fig. 6 shows results of simulations yielding fluorescence transfers closely approximating experimental CPP transfer fluorescence data for both SAOS-2 and fibroblasts, and this concordance was seen making biologically reasonable assumptions for relevant variables. Median fluorescence levels of donor and receptor cells are shown in Table 1, and demonstrate similarity between experimental and simulated results. Relative fluorescence transfer from fibroblasts to SAOS-2 was greater compared with that from SAOS to fibroblasts in both simulations and by experiment (Table 1).

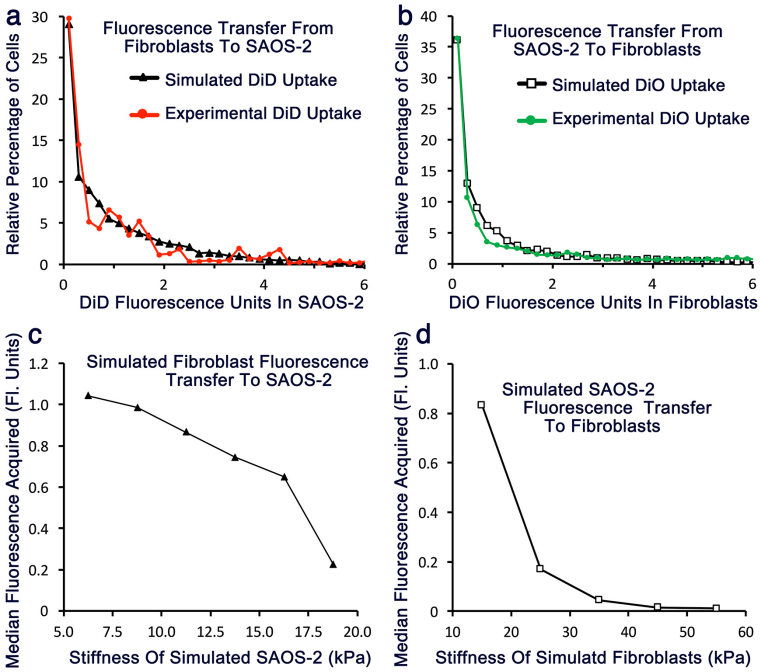

Figure 6. *Graphs comparing exchange of fluorescence between SAOS-2 and fibroblasts observed by experiment (Figs. 4 and 5), with that calculated by numerical simulations for 5000 recipient SAOS-2 or fibroblasts (a,b), and the relationship between recipient cell stiffness and fluorescence uptake (c,d).* ***(a,b)*** *There was good concordance between experimental observations and results of numerical simulations, applying simulation conditions where: the number of donor fibroblasts any given recipient SAOS-2 could interact with ranged from 1 to 3 (1 to 3 for fibroblast recipients); the number of exchange events between individual donor fibroblasts and recipient SAOS-2 cells ranged from 0 to 2, (3 to 8 for recipient fibroblasts); the rate of cell-projection retraction ranged from 0.5 to 1.4 μm/s for donor fibroblasts, (1 to 5 μm/s for donor SAOS-2); the proportion of maximal possible time for individual transfer events applied ranged from 0 to 0.9 for fibroblast cell-projection retraction (0.6 to 0.9 for SAOS-2 cell-projection retraction); the length of donor cell-projections from donor fibroblasts ranged from 5 to 120 μm, (40 to 90 μm from donor SAOS-2); the radius of fibroblast donor cell-projections was from 0.55 to 1.75 μm, (0.7 to 2.5 μm for donor SAOS-2); and the viscosity of cytoplasm ranged from 1.5 to 4.0 mPa.s for both donor fibroblasts and SAOS-2.* ***(c,d)*** *There was an inverse relationship between SAOS-2 stiffness and median fluorescence acquired by CPP (c), with a similar result for fibroblasts receiving SAOS-2 fluorescence (d) ($p < 0.0001$, Mann Whitney U Test).*

Consistent with experimental data (Fig. 4), there was an inverse relationship between stiffness and transfer from both fibroblasts to SAOS-2, and also from SAOS-2 to fibroblasts (Fig. 6c,d). Results of simulations thus satisfied all predictions from the mathematical model.

Pressures required for these transfers were generally modest: 1.15×10^{-8} Pa to 212 Pa, with a median value of 0.668 Pa for transfer from fibroblasts to SAOS-2; and 8.98×10^{-11} Pa to 37.3 Pa, with a median value of 0.144 Pa for transfer from SAOS-2 to fibroblasts. Only 2.91% of calculated pressure values were over 10 Pa for transfer from fibroblasts to SAOS-2, while only 0.40% of calculated pressures were over 10 Pa for transfer from SAOS-2 to fibroblasts. The predominantly low pressures calculated to account for fluorescence transfer, support plausibility for CPP.

Table 1. Median fluorescence levels from experimental observations and simulations

	Median Fluorescence per Cell (Fluorescence Units)			Receptor Fluorescence / Donor Fluorescence	
	Donor Cells	Experimental Receptor Cells	Simulated Receptor Cells	Experimental	Simulated
Red (DiD) Fluorescence	16.904	0.641	0.630	0.038	0.037
Green (DiO) Fluorescence	31.849	0.504	0.414	0.016	0.013

Overall fluorescence levels for simulated receptor cells was comparable to that seen in experimental results. When expressed as ratios relative to donor cell fluorescence, fibroblasts which were the receptors for green DiO fluorescence, had lower uptake relative to red DiD fluorescence by SAOS-2 receptor cells. Proportionate uptake was similar between simulation results and experimental data, with fluorescence uptake of SAOS-2 being 2.40 fold that of fibroblasts (0.038/0.016) by experiment, and 2.81 fold that of fibroblasts by simulation (0.037/0.013).

Simulations predicted large proportional volume transfers between cells. Data on volume exchange were expressed as percentages relative to the average volume of a single Receptor Cell B SAOS-2 or fibroblast. Table 2 shows results for volume transfers in the same simulations illustrated in Fig. 6. Most simulated cells in recipient populations accepted appreciable volumes of donor cell cytoplasm. Simulated proportional volume transfers to fibroblasts were generally lower than those calculated for SAOS-2 (Table 2).

Discussion

All predictions that follow from the CPP hypothesis and mathematical model were satisfied by either experiment or simulations. Taken together, these differing data support CPP as a previously unrecognized mechanism for inter-cellular cytoplasmic exchange, and we suggest the current work forms a reasonable theoretical framework for further investigation.

TNT differ fundamentally from the cell-projections observed to be responsible for CPP in the current study. Whereas cell-projections mediating CPP presented as transient, short, and branching structures, mechanically supported by the culture surface or cells; TNT often persist hours, extend long distances, are non-branching, and are suspended free above the culture surface [11,12,16,19-23]. While delivery of surface signals and directed migration are known roles for specialized filopodia [33], cytoplasmic transfer via cell-projections in the size range of filopodia seems a novel function. Some precedent is, however, established by filopodial transfer of melanosomes, but precise details of melanosome transfer remain uncertain and phagocytosis of shed melanosomes may occur [34-36]. It would be interesting to determine if CPP contributes to melanosome transfer. Similarly, the mechanism whereby mitochondria are transferred between mammalian cells remains unclear [5-10,18], and we speculate that CPP contributes to this important process.

We have separately demonstrated TNT in MC [20-22], and also showed increased TNT on exposure to exosomes [25], but consistent with our initial report [1], neither TNT or exosomes could account for the current observations. Uptake of fibroblast label by MC was not only inconsistent with exosome or TNT transfer, but was also not

Table 2. The proportionate percentage distribution of recipient SAOS-2 and fibroblasts, according to the volume acquired from the opposing cell type in simulated co-culture generating fluorescence profiles approximating those seen by experiment, expressed as percentages relative to the average volume of the respective recipient cell type.

% Volume Relative to Average Recipient Cell	Simulated SAOS-2 Number	% Relative to All Simulated SAOS-2	% of Simulated SAOS-2 with Transfer over Threshold	Simulated Fibroblast Number	% Relative to All Simulated Fibroblasts	% of Simulated Fibroblasts with Transfer over Threshold
0 to < 1	1301	26.02	100	2062	41.26	100
1 to < 3	925	18.5	73.98	1274	25.46	58.74
3 to < 5	661	13.22	55.48	523	10.46	33.28
5 to < 7	455	9.1	42.26	263	5.26	22.82
7 to < 9	376	7.52	33.16	176	3.54	17.56
9 to < 11	312	6.24	25.64	135	2.58	14.02
11 to < 13	232	4.64	19.4	141	2.82	11.44
13 to < 15	205	4.1	14.76	110	2.26	8.62
15 to < 17	164	3.28	10.66	88	1.76	6.36
17 to < 19	110	2.2	7.38	80	1.6	4.6
19 to < 21	64	1.28	5.18	52	1.08	3
21 to < 23	64	1.28	3.9	26	0.52	1.92
23 to < 25	45	0.9	2.62	21	0.42	1.4
25 to < 27	23	0.46	1.72	19	0.38	0.98
27 to < 29	21	0.42	1.26	16	0.32	0.6
29 to < 31	15	0.3	0.84	4	0.08	0.28
31 to < 33	6	0.12	0.54	0	0	0.2
33 to < 35	11	0.22	0.42	3	0.06	0.2
35 to <37	3	0.06	0.2	4	0.08	0.14
37 to <39	1	0.02	0.14	0	0	0.06
39 to <41	3	0.06	0.12	2	0.04	0.06
41 to <43	0	0	0.06	0	0	0.02
43 to <45	2	0.04	0.06	0	0	0.02
45 to <47	1	0.02	0.02	0	0	0.02
47 to <49	0	0	0	1	0.02	0.02
Total	5000	100		5000	100	

Simulations predicting fluorescence profiles for recipient cells similar to experimental results (Fig. 6), also predicted transfer of appreciable volumes of cytoplasm to recipient cells. 55.5% of simulated SAOS-2 had over 3%, and 5.2% of SAOS-2 had over 19% volume acquired from simulated fibroblasts. Consistent with occasional experimentally observed SAOS-2 with very high fibroblast DiD labelling, 10 simulated SAOS-2 cell acquired between 35% and 47% of their volume from simulated fibroblasts. Simulated fibroblasts also acquired appreciable cytoplasm from simulated SAOS-2, but this was generally less compared with exchange in the reverse direction.

accounted for on basis of non-specific DiD (red) label diffusion, or phagocytosis of fibroblast cell fragments. In addition, the deep grooving of MC by fibroblast cell-projections was indicative of a significant difference in cell stiffness, further confirmed by AFM and correlated with the extent of cytoplasmic exchange. The asymmetry in exchange seen experimentally between fibroblasts and SAOS-2 was consistent with our earlier published observations [1].

We earlier noted phenotypic changes associated with intercellular cytoplasmic and membrane transfer [1,14,15], and suggest CPP as playing a role in this. In addition, the appreciable volumes of SAOS-2 cytoplasm transferred to fibroblasts in simulations, suggests a possible role of CPP in development of cancer-associated fibroblasts, which are increasingly recognized as important for cancer development [37].

Numerical modelling permitted estimation of the volumes of cytoplasmic transfer required to account for exchange in co-culture, previously not possible due to diversity in donor cell fluorescence. The appreciable relative volume transfers seen in Table 2 were consistent with the high fluorescence exchange visually apparent in experiments[1] (Figs. 1,3, 4).

Although we do believe our approach to mathematical modeling is reasonable, there are some aspects that bear further discussion. As discussed below (materials and methods), the formal definition of Young's modulus and 'stiffness' as it relates to Hookean elastic materials, should not be directly applied to cell stiffness measurements acquired by AFM. Instead, we interpret the Young's Modulus measurements acquired by AFM in the current study, as indicative of a constant resistance to force. However, the term 'cell stiffness' is widely accepted, so we have persisted with use of this tern for the sake of communication.

AFM measurements are of necessity made from outside the measured cell, and this differs fundamentally from stiffness as may exist but cannot be readily measured, from within the cell. The plasma membrane can be likened to the surface of a tent tethered to an underlying framework, where the force of resistance to downward pressure against the framework is different to that experienced when pushing from within. It is reasonable, however, to assume that the force experienced from both directions is correlated in a broadly linear fashion. From this, while there is no clear alternative, it nonetheless seems reasonable to apply AFM stiffness measures in our mathematical model. That the cell stiffness correction factor applied, Z=(1/median stiffness value of all cells in the simulation) yielded intelligible results, with tc neither negative or compressed against Lo/U (Fig. 1e) for simulation with median stiffness cells (Fig. 4e), seems to support our interpretation for cell stiffness.

Cytoplasmic viscosity is non-uniform and dependent on scale, with viscosity being very low but varying across micro-volumes of the cell dependent on contents, and increasing to high levels when measured at the whole cell level due to the admixture of organelles and cytoskeletal elements [38-40]. At the scale modeled in the current study, cytoplasm has viscosity ranging upwards from that close to water, in the ranges approximately from 1 to 4 mPa.s [38,40], and this is reflected by the values we used for this variable. Turbulent flow is near impossible in the range of radius values used, lending confidence to use of the Hagen-Poiseuille equation in our model. The effect of organelles suspended in cytoplasm is, however, more difficult to anticipate. We suggest that although cytoplasm itself at the scale studied may have very low viscosity in the order of 1.5 mPa.s, that by including higher viscosity values in simulations, we have made reasonable accommodation for the effect of suspended organelles.

In preliminary simulations not shown, we assumed a normal distribution between target minima and maxima for variables other than stiffness and fluorescence, and observed 'a central hump' in the resulting simulated fluorescence profiles, inconsistent with experimental fluorescence. Weakening the central tendency by spreading the distribution of variables to a flattened profile, achieved simulation results more in keeping with experimental data, and this suggests a 'flat distribution' for key variables *in-vivo*. Confirmation of this inference awaits improved structural and temporal resolution of events in living cells. Modest divergence of simulated from experimental results, likely reflects limitations inherent to the model, including possible skewedness and unknown dependencies between variables.

While acknowledging the limitations of our analysis discussed above, we do feel it is reasonable to advance our hypothesis of CPP between mammalian cells. Not only does CPP seem to be a previously unrecognized biological process, but our earlier work suggests CPP results in significant phenotypic change [1,15], and this has direct relevance to generation of tumor cell diversity and hence progression of malignancy.

Not addressed in the current work, is the basis for formation of the transient inter-cellular cytoplasmic continuities through which cytoplasm must pass between cells. We have no current data on this point, but speculate that these may form through membrane fusion mechanisms.

It is unlikely that CPP would be confined to interactions between fibroblasts and MC, while we earlier reported uptake of cytoplasm from smooth muscle cells by MC [1]. Cancer only rarely seems to generate truly new biology, but instead appears to pervert established biological mechanisms. For these reasons, we think it highly likely that CPP plays an important role in cell differentiation and phenotypic control in other biological settings including embryogenesis, development, inflammation and wound healing, consistent with reports of intercellular exchange by both reported and as yet unresolved mechanisms [1-16,18-25,34-36]. We believe our current work forms a useful platform from which to explore these further interesting possibilities.

Materials and Methods

Materials. All culture media including M199, DMEM-α Trypsin (0.25%)-EDTA (0.02%) and phosphate buffered saline (PBS), as well as Penicillin (10,000 U/ml)-Streptomycin (10,000 μg/ml) concentrate solution were prepared and supplied by the Memorial Sloan-Kettering Cancer Centre Culture Media Core Facility (New York, NY). Amphoteracin B was purchased from Life Technologies (Grand Island, NY). Gelatin was from TJ Baker Inc (Philipsburgh, NJ). Bovine serum albumin was from Gemini Bioproducts (West Sacramento, CA). Falcon tissue culture flasks, Atomic Force Microscopy (AFM) dishes and centrifuge tubes were purchased from BDBiosciences (Two Oak Park, Bedford, MA). Culture well coverslips were from Lab-Tek (Rochester, NY). Human dermal fibroblasts were from The Coriell Institute (Camden, NJ). SAOS-2 osteosarcoma cells were from the American Type Culture Collection (VA, USA). MM200-B12 melanoma cells from The Millennium Institute (Westmead, NSW, Australia). The fluorescent labels 1,1'-dioctadecyl-3,3,3',3'-tetramethylindodicarbocyanine perchlorate (DiD), 3,3'-dioctadecyloxacarbocyanine perchlorate (DiO), and Bacmam 2.0 Cell lights Nuclear-GFP baculovirus, were purchased from Molecular Probes by Life Technologies (Grand Island, NY) in the form of DiD and DiO Vybrant cell labelling solutions, and BacMam Cell Light transfection reagent. Paraformaldehyde (PFA) solution (32%) was purchased from

Electron Microscopy Supplies (Hatfield, PA). A 6.1 μm spherical polystyrene AFM probe was purchased from NanoAndMore (Lady's Island, SC). The anti-fade reagent used was supplied by the Molecular Cytology core facility at Memorial Sloan Kettering Cancer Center.

Cell culture and fluorescent labelling. The antibiotics penicillin (100 U/ml), streptomycin (100 μg/ml) and amphotericin B (2.5μg/ml) were used throughout all cell culture. Fibroblasts were always cultured on gelatin coated surfaces (0.1% in PBS) in DMEM-α (15% FCS). The osteosarcoma cells SAOS-2 were cultured in M199 (10% FCS), while MM200-B12 were cultured in DMEM-α (10% FCS). Cells were harvested using trypsin-EDTA, into FCS to neutralize trypsin, and pelleted by centrifugation before passage at a ratio of 1 to 3. All cell culture was performed at 37° C under CO_2 (5%) and at 100% humidity.

Labelling solutions of DiD (1mM) and DiO (2mM) were prepared in DMEM-α with 10% FCS, and applied to cells for 30 minutes in the case of DiD, while DiO was applied for 1 hr. Cells were then washed twice with PBS before overnight culture with DMEM-α with BSA (4%) followed by two further washes with PBS to ensure removal of any unbound label. In some experiments, MM200-B12 were transfected with green fluorescent protein (GFP) expressing baculovirus, by culturing overnight 6 x 10^6 MM200-B12 in a 6 well tissue culture plate well in DMEM-α (FCS 10%) with 2.4 x 10^7 baculovirus particles.

Co-culture conditions. Cells were cultured on gelatin (0.1% in PBS) coated surfaces. Fibroblasts were seeded at from 1 to 2 x 10^4 cells per cm^2 into 25cm^2 AFM culture plates, appropriate for use in the AFM as earlier described [26], or into culture well coverslips, and allowed to adhere overnight before labelling with DiD as outlined above. MC were seeded at near confluence in 25 cm^2 flasks in M199 with FCS (10%) and allowed to adhere overnight, before labeling with DiO as outlined above. MC were then harvested with trypsin-EDTA and seeded in DMEM-α with BSA (4%) at a culture density of 4 x 10^4 cells per cm^2 for up to 24 hr co-culture.

Confocal microscopy. Before examination of co-cultures, control monolayers labelled with DiO, DiD or GFP alone were used to establish fluorescence conditions minimizing background and cross-fluorescence. Fibroblast were always pre-labelled with DiD (red). Eight separate visual fields of MM200-B12 pre-labelled with GFP (green) co-cultured with fibroblasts were recorded for 25 hr at 3 min intervals, representing 1.13 mm^2 culture surface area and observing 40 fibroblasts and 71 MM200-B12. Nine further separate visual fields of DiO (green) pre-labelled MM200-B12 co-cultured with fibroblasts were recorded for 8 hr 15 min at 5 min intervals and at slightly higher magnification, representing 0.76 mm^2 culture surface area and observing 90 fibroblasts and 106 MM200-B12. At the conclusion of time-lapse recordings, monolayers were fixed with paraformaldehyde as earlier described [26].

Confocal microscopy including time-lapse was performed using a Zeiss LSM 5Live line-scanning confocal microscope. ImageJ open source software (contributors listed at http://imagej.net/Contributors) was used to analyze images from both fixed cells and time-lapse records. Flattened optical projections and individual optical sections were visualized in channels for both DiD and DiO alone and together.

Atomic force and fluorescence microscopy to establish cell stiffness and fluorescence values. AFM is widely used to evaluate cell stiffness, described as Young's modulus in SI units of N/m^2 or Pa, and is calculated from AFM recordings of force versus indentation curves using the Hertz model as described elsewhere [26,41]. AFM cell surface stiffness is usually established by obtaining single measurements over the nuclei of multiple cells [42-44]. Our interest, however, lies in global and cytoplasmic cell stiffness, and for this reason we earlier developed a scanning AFM approach that generates stiffness fingerprints, sensitive to nuanced differences between cell populations, and encompassing the entire upper surface of cultured cells. Observations from stiffness fingerprints important for the current study, are that cell surface microdomains vary greatly in stiffness across the surfaces of individual cells, and that median values for microdomain stiffness provide a reasonable and reliable measure for global cell stiffness [26]. Stiffness fingerprints were used in the current study to examine the relationship between cell stiffness and fluorescence exchange, and also to inform CPP numerical modeling.

Monolayers were fixed with paraformaldehyde as earlier described [26], and stored in PBS at 4º C for combined fluorescence-AFM recordings. An Asylum Research MFP-3D-BIO atomic force microscope coupled with a Zeis Axio Observer A1 fluorescence microscope was used. There was random selection of cells for examination. Bright field and fluorescence images for both DiO and DiD channels were recorded, prior to AFM scanning to establish stiffness fingerprints of individual cells using an approach detailed in our earlier work [26].

In brief, a 6.1 μm spherical polystyrene probe was used, while the manufacturer provides guarantee of probe size by scanning electron microscopy. The precise Z-distance calibration of deflection, as well as the cantilever stiffness was established by InvOLS and thermal tune calibration as detailed elsewhere [26], and a slow indentation velocity of 3.5 μm/s was used to reduce viscous effects. A trigger point for retraction was defined at 25 nm deflection, so that indentation depth depended on stiffness of the area measured, while indentation depth was usually between 100 nm and 500 nm. 16 x 16 points of force curves were collected over 50 μm x 50 μm areas. The automated software provided by the manufacturer of the instrument (Asylum Research, Software Version IX) was used to establish a plane fit, and height measurements were made relative to the lowest point measured, assumed to represent the plastic cell culture surface as detailed elsewhere [26]. The AR software was used to provide Young's modulus for each point as calculated by the Hertz model [26,41], and all data was then exported to Excel software (Microsoft, Redmond, WA). Height maps, bright field and fluorescence images were compared to localize discrete AFM measurement points to individual cells, while as detailed in our earlier work, sites with height values at or below 0.8 μm were excluded to avoid effects from the underlying culture surface [26,45,46].

Morphometric analysis establishing the extent of fluorescence exchange between SAOS-2 and fibroblasts, and correlation of this with cell stiffness. AFM scans only rarely sampled the full extent of individual cells. Nonetheless, those cells for which an appreciable number of AFM data points were available, and for which it was also possible to establish numerical fluorescence values as detailed below, were analyzed to correlate cell stiffness and height with cell type and the extent of fluorescent label exchange. Fibroblasts were recognized as large elongated cells heavily labelled with DiD (red), while SAOS-2 were recognized as DiO (green)

positive cells that were usually smaller and more round compared with fibroblasts. DiD (red) fluorescence in SAOS-2 was quantitated to further divide these cells into two groups, being those which had high as opposed to low levels of fibroblast label.

Quantitation of fluorescence labelling and cell surface area profile was performed as follows. Fluorescence images of individual SAOS-2 and fibroblasts for which appreciable AFM measurements were available, were divided into separate RGB channels, and the cell surface profiles segmented in the blue channel only to ensure that data in red and green channels were not affected by the cell segmentation procedure. Images of individual cells derived by recombining channels where then processed using Image J software to relate total cell surface area to the total DiD or DiO label present. The individual steps through which this was achieved in ImageJ were: separation of channels into red, green and blue; establishment of thresholds for detection of red, green and blue; detection of areas above threshold for red, green and blue, and overlapping of these to create single areas for analysis; and quantitation of red and green in the defined areas with expression of this as average units of red or green fluorescence per pixel, permitting assignation of individual SAOS-2 as being in either the 'high' or 'low' fibroblast labelling group.

Median AFM stiffness values were determined for individual fibroblasts and SAOS-2, permitting an initial impression of the relationship between cell stiffness and cell type defined as above, but the limited sampling at the level of individual cells restricted capacity to evaluate results in a statistically meaningful way. The stiffness fingerprint method recently published [26], in which height and stiffness data from multiple cells are pooled and displayed as scattergrams of height versus stiffness, overcomes this difficulty, and was applied in the current study. Statistical significance of differences in stiffness and height between fibroblasts, SAOS-2 with high fibroblast label, and SAOS-2 with low fibroblast label, was determined using the two-tailed Mann Whitney U Test in Prism 6.0e software (GraphPad Software Inc, La Jolla, CA).

Derivation of equations describing CPP.

General features of the model. CPP is described mathematically for a simple two chamber hydrodynamic system joined by a cylindrical connector (Fig. 1b,c). Calculations are based on the well described Hagen-Poiseuille relationships, where resistance to flow in a cylindrical tube (ρ) is given by equation (2), and the flow rate (Q) of a Newtonian fluid of viscosity (η) through a cylindrical tube of length (L) with radius (r), due to a pressure difference (ΔP) as per equation (3) [32].

$$\rho = \frac{8\,\eta}{\pi \cdot r^{4}} \tag{2}$$

$$Q = \frac{\Delta P}{\rho \cdot L} = \frac{\Delta P \cdot \pi \cdot r^{4}}{8\,\eta \cdot L} \tag{3}$$

Important simplifying assumptions. Because the fluid volumes exchanged between cells are very small, it is reasonable to assume negligible bulk modulus effect, and the cytoplasm exchanged between cells is assumed to behave as an incompressible Newtonian fluid. Pascal's law predicts that any pressure change within a confined Newtonian fluid is transmitted throughout the fluid such that the change is the same throughout [31]. Pascal's law thus renders modeling of fluid flow in the current study

independent of non-topological geometric details, so that bends and connection to blind-ending branches, should have little or no effect on quantitative results. Notably, the hydraulic system illustrated in Fig. 1 is not confined, but consists instead of two 'open' halves, each of which operates against a separate constant force, and hence each of which has a separate ΔP (ΔP_A and ΔP_B for Donor and Receptor Cells respectively), as also demanded by Pascal's law [31].

A number of further assumptions are made in derivation of the below described mathematical model, which greatly reduce complexity of calculation and also seem reasonable in light of the limited data available. For example, in absence of more detailed spatial and temporal observations, we assume a constant rate for retraction of cell-projections, and a cylindrical form for the cell projections.

Only flow into Receptor Cell B (Q_B) is calculated in the current study, since it is only Q_B which will deliver cytoplasm to the opposing cell (Fig. 1). Also, since maximum pressure is located within of the retracting cell-projection at position Po (described below, Fig. 1diii), there is no actual cytoplasmic flow at Po which acts as an effective 'syringe plunger' for flow in both cell directions. ΔP is exhausted upon complete retraction, thus limiting the total possible volume of flow to that of the cell-projection.

The cell surface is non-elastic. In addition, unlike an elastic Hookean spring, the resisting force of a cell against incoming cytoplasmic fluid flow is assumed to be constant, more in keeping with the behavior of a hydraulic piston that works against a constant friction or constant weight, as illustrated in Fig. 1c.

In an elastic system, Young's modulus relates the force applied across a surface area to achieve a given proportional displacement, and could be interpreted in context of the current model as shown in Fig. 1c and equation (4), where Young's modulus = stiffness = S, Force = F, Area of the piston = Ar, and vertical displacement of the piston = d, indicating relevant Surfaces A or B with respective subscripts ($S, F, Ar, d_{A \text{ or } B}$) [26,47].

$$S_A = \frac{F_A/Ar_A}{d_A} \qquad S_B = \frac{F_B/Ar_B}{d_B} \tag{4}$$

Young's modulus thus relates specifically to elastic Hookean materials. However, despite the wide use of Young's modulus as an AFM measure for cell surface stiffness, strict application of this value to the current model is not justifiable.

Firstly, Young's modulus as determined from AFM data is a calculated value, established by fitting via the Hertz model [26,41]. Also, cells do not have a homogeneous structure, as normally required for true elastic behavior. Further, although AFM cell stiffness fingerprints permit meaningful comparison between cells, such stiffness fingerprints of necessity measure resistance to displacement from the outside of fixed cells [26]. This is different to the resistance to force more relevant to the current study, but not readily measured, being that from the inside of living cells.

From the above, it seems more reasonable to accept AFM determined stiffness values as indicative of the resistance of the surface to displacement by force, but not as absolute measures of elasticity. Also, given the structure of the cell surface as a membrane tethered to an underlying horizontal network of cytoskeletal fibres, it seems reasonable to assume that the cell surface force resisting injection of fluid into cells during CPP is constant.

Although we do not accept true Hookean elasticity of the cell surface, and hence must reject the formal definition of 'stiffness' as it applies to cell measurements by AFM, we acknowledge that the term 'stiffness' is entrenched in the literature in this regard. For this reason, we will persist in use of the word 'stiffness' in the current work, to indicate that constant force exerted by the cell in opposition to receiving cytoplasm via CPP.

It seems reasonable to assume only modest effect of the simplifying assumptions outlined above, in diverging the calculated estimations made in the current study, from events in-vivo.

Modification of the Hagen-Poiseuille equation accommodating differences in cell stiffness. Distribution of fluid during retraction of the cell-projection in Fig. 1b,c is influenced by the relationship between stiffness of Donor Cell A (S_A) and Receptor Cell B (S_B), and this requires modification of the relationships described in equations (2 and 3) for calculation of that portion of total flow distributed to Receptor Cell B (Q_B).

Fig. 1di shows a cylindrical tube of known length ($L_{(t)}$) at time (t) as measured from '0' at it's origin which is closed and marked to the left, and in which there is contraction at a constant rate (U), as indicated in equation (5).

$$U = \frac{L(t)}{dt} \tag{5}$$

The tube contains a Newtonian fluid, and is divided into n cylinders of equivalent length (Δx) as shown in equation (6), indexed from n=1 to n (Fig. 1dii).

$$\Delta x = \frac{L(t)}{n} \tag{6}$$

Because the tube undergoes a constant contraction, each cylinder also contracts by $U\Delta t/n$ to displace a volume of fluid (ΔV) as in equation (7), where Ca is the cross-sectional area of the tube.

$$\Delta V = \frac{Ca \cdot U(\Delta t)}{n} \tag{7}$$

In this way, each cylinder donates an equivalent volume (ΔV) and flow rate increment ($\Delta q = \Delta V/\Delta t$), to the total flow rate of the cylinder as in equation (8), substituting for n from equation (6).

$$\Delta q = \frac{Ca \cdot U}{n} = \frac{Ca \cdot U \cdot \Delta x}{L(t)} \tag{8}$$

Rearrangement of equation (8) gives equation (9).

$$\frac{\Delta q}{\Delta x} = \frac{Ca \cdot U}{L(t)} \tag{9}$$

As $n \to \infty$, $\Delta x \to 0$, so that the flow rate at x, (Q(x)), is given by equation (10).

$$Q(x) = \int_0^x \frac{Ca \cdot U}{L(t)} dx \ = \frac{Ca \cdot U \cdot x}{L(t)} \tag{10}$$

Note that the flow rate at the end of the tube where x=L(t) is CaU as expected (Fig. 1dii).

Let ρ be the resistance per unit length as given in equation (2), so that the resistance offered by any given small cylinder comprising the cell-projection (ΔR) is given by equation (11), and the pressure drop across the cylinder ($\Delta P_{\Delta X}$) is given by equation (12) as per equations (3 and 8).

$$\Delta R \ = \ \rho \cdot \Delta x \tag{11}$$

$$\Delta P_{\Delta X} \ = \Delta q \cdot \Delta R \ = \frac{Ca \cdot U}{n} \cdot \rho \cdot \Delta x \tag{12}$$

The pressure drop at any cylinder k and L=x is given by equation (13), which can be rearranged to equation (14).

$$\Delta P_X \ = \frac{k \cdot Ca \cdot U}{n} \cdot \rho \cdot \Delta x \tag{13}$$

$$\frac{\Delta P_X}{\Delta x} \ = \frac{k \cdot Ca \cdot U \cdot \rho}{n} \tag{14}$$

Substituting for 1/n from equation (6), and recognizing that x= kΔx gives equation (15).

$$\frac{\Delta P}{\Delta x} \ = \ \frac{Ca \cdot U \cdot \rho \cdot k \cdot \Delta x}{L(t)} \ = \ \frac{Ca \cdot U \cdot \rho \cdot x}{L(t)} \tag{15}$$

Allowing Δx → 0, gives the expressions in equation (16).

$$\frac{\Delta P}{\Delta x} \ \rightarrow \ \frac{dP(x)}{d(x)} \ = \ \frac{Ca \cdot U \cdot \rho \cdot x}{L(t)} \tag{16}$$

From this, the pressure drop P(x) at x, is given as expressions in equation (17).

$$P(x) = \int_0^x \frac{Ca \cdot U \cdot \rho \cdot x}{L(t)} dx \ = \frac{Ca \cdot U \cdot \rho \cdot x^2}{2 \cdot L(t)} \tag{17}$$

Consider the above outlined system now duplicated, and one of these elements to be rotated so that the two tubes now abut end to end, with the origin x=0 being identical for both. This now represents a cell-projection joining Donor Cell A 'to the left', with Receptor Cell B positioned 'to the right'. The origin represents a point in the cell-projection (Po) where during contraction of the cell-projection, there is maximum pressure and no flow, the origin functioning as an effective 'syringe stop' for flow in both directions. The length of tube between the origin and Donor Cell A is L_A, and that to Receptor Cell B is L_B (Fig. 1diii), giving equation (18) for length at time t.

$$L(t) \ = \ L_A(t) + L_B(t) \tag{19}$$

The tube is open to Cells A and B, and flow out of the tube in both directions is resisted by constant forces F_A and F_B in Cells A and B respectively (Fig. 1diii). These forces are proportionate but not identical to the measured median cell stiffness of the Donor and Receptor cells (S_A and S_B), so that it may be helpful to read 'S' for 'F' when making reference to Fig. 1.

Noting that U is constant, equation (18) gives equation (19) following simplification, where: $U = L/t$, $U_A=L_A/t$, and $U_B=L_B/t$.

$$U = U_A + U_B \tag{19}$$

The relationships in equation (20) follow from the above.

$$\frac{U_A}{U} = \frac{L_A(t)}{L(t)} \qquad \frac{U_B}{U} = \frac{L_B(t)}{L(t)} \tag{20}$$

If PMax is the pressure at the origin (O), then from equation (17), the pressure at x_B going to the right (P_R) is given by equations (21), ultimately reaching and being balanced by the hydrodynamic force resisting flow by Cell B (F_B) to the right, with pressure at x_A going left (P_L) reaching the hydrodynamic force resisting flow by Cell A (F_A) to the left (equation (21)), as illustrated in Fig. 1diii.

$$P_R(x) = PMax - \frac{Ca \cdot U_B \cdot \rho \cdot x_B^2}{2 \cdot L_B(t)} \qquad P_L(x) = PMax - \frac{Ca \cdot U_A \cdot \rho \cdot x_A^2}{2 \cdot L_A(t)} \tag{21}$$

Since $L_A = x_A$, and $L_B = x_B$, equations (21) simplify to equations (22).

$$P_R(x) = PMax - \frac{Ca \cdot U_B \cdot \rho \cdot L_B(t)}{2} = F_B \qquad P_L(x) = PMax - \frac{Ca \cdot U_A \cdot \rho \cdot L_A(t)}{2} = F_A \tag{22}$$

Rearrangement of equations (22) gives equation (23).

$$F_A + \frac{Ca \cdot U_A \cdot \rho \cdot L_A(t)}{2} = F_B + \frac{Ca \cdot U_B \cdot \rho \cdot L_B(t)}{2} \tag{23}$$

Substituting for L_A from equation (18) gives equation (24).

$$F_A + \frac{Ca \cdot U_A \cdot \rho \cdot (L(t) - L_B(t))}{2} = F_B + \frac{Ca \cdot U_B \cdot \rho \cdot L_B(t)}{2} \tag{24}$$

Substitution for: U_B from equation (19); U_A/U from equation (20); and L_A from equation (18), gives equation (25) for L_B.

$$L_B(t) = \frac{F_A - F_B}{Ca \cdot U \cdot \rho} + \frac{L(t)}{2} \tag{25}$$

The algebraic relationships leading to equation (25) apply equally to generate equation (26).

$$L_A(t) = \frac{F_B - F_A}{Ca \cdot U \cdot \rho} + \frac{L(t)}{2} \tag{26}$$

From equations (25 and 26), when $F_A=F_B$, then $L_A(t) = L_B(t) = L(t)/2$, and both cells receive equivalent flow as expected from symmetry of the system. When $F_A>F_B$,

a time is reached when $L_A(t)$ reaches 0 and all remaining flow is to the right, and Receptor Cell B receives more flow than Cell Donor Cell A (Fig. 1diii), while the reverse applies when $F_A<F_B$.

Equation (27) follows from equation (10).

$$Q_B = \frac{Ca \cdot U \cdot L_B(t)}{L(t)} \tag{27}$$

To establish the total flow transferred to Receptor Cell B ($Q_B(t)$), $L_B(t)$ from equation (25) is substituted into equation (27), which with simplification gives equation (28).

$$Q_B = \frac{F_A - F_B}{\rho \cdot L(t)} + \frac{Ca \cdot U}{2} \tag{28}$$

Because U is constant, L(t) is given by equation (29), and substitution for L(t) in equation (29) gives equation (30).

$$L(t) = L_0 - U \cdot t \tag{29}$$

$$Q_B = \frac{F_A - F_B}{\rho \cdot (L_0 - U \cdot t)} + \frac{Ca \cdot U}{2} \tag{30}$$

Note that equation (30) can only apply while $(F_A\text{-}F_B)/\rho(L_0\text{-}Ut) \leq CaU/2$, because at this point $L_A = 0$ and $L_B = L$ where $S_A>S_B$, with all flow being to the right into Receptor Cell B at a rate of $Q_B = CU$; while where $S_A<S_B$, $L_B=0$ and $L_A=L$ and all remaining flow is to the left into Donor Cell A. Let the time at which this occurs be tc to give equation (31).

$$\frac{F_A - F_B}{\rho \cdot (L_0 - U \cdot tc)} = \frac{Ca \cdot U}{2} \tag{31}$$

Expansion, rearrangement and simplification of equation (31), gives equation (32) for tc, where the absolute value of second term on the right is required to accommodate occasions when $F_A<F_B$.

$$tc = \frac{L_0}{U} - \left| \frac{2(F_A - F_B)}{Ca.\rho \cdot U^2} \right| \tag{32}$$

Fig. 1e is a graphical representation of Q_B from t = 0 to t = L_0/U at which time $L_B = 0$ and no further flow Q_B is possible. When $F_A>F_B$, equation (30) for Q_B applies for $t \leq tc$, and $Q_B = CaU$ for $tc < t < L_0/U$. Increasing values of $(F_A\text{-}F_B)$ reduce tc, while as $(F_A\text{-}F_B)$ approaches 0, tc approaches L_o/U and Q_B approximates CaU/2 from above for increasing time when $F_A>F_B$, and from below when $F_A<F_B$. Also, when $F_A<F_B$, equation (30) predicts that Q_B approaches 0 as t approaches tc, after which Q_B remains 0 due to exhaustion of L_B to 0 at tc. Let the total volume transferred to Receptor Cell B be V_B.

Where $F_A>F_B$, the relationships outlined above determine $V_B(t)$ as per equation (33).

$$V_B(t) = \int_0^{tc} \left(\frac{Ca \cdot U}{2} + \frac{F_A - F_B}{\rho \cdot (L_0 - U \cdot t)}\right) dt + \int_{tc}^{L_0/U} (Ca \cdot U)\ dt \tag{33}$$

Similarly, where $F_A < F_B$, $V_B(t)$ is given by equation (34).

$$V_B(t) = \int_0^{tc} \left(\frac{Ca \cdot U}{2} + \frac{F_A - F_B}{\rho \cdot (L_0 - U \cdot t)}\right) dt \tag{34}$$

Also, where $F_A = F_B$, $V_B(t)$ is given by equation (35).

$$V_B(t) = \int_0^{L_0/U} \left(\frac{Ca \cdot U}{2}\right) dt \tag{35}$$

To aid integration in equations (33 and 34), define w(t) as in equation (36), such that when t = 0, w = L_0; and when t = tc, w = L_0-Utc.

$$w(t) = L_0 - U \cdot t \tag{36}$$

Differentiating equation (36) gives equation (37).

$$dw = -U \cdot dt \tag{37}$$

From this, the second term in equations (33 and 34) can be expressed and integrated with regard to w as in equation (38), where ln(w) is the natural logarithm of w. Substitution of equation (36) into equation (38) gives the expression in equation (39).

$$-\frac{1}{U}\int_{L_0}^{(L_0 - U \cdot tc)} \left(\frac{F_A - F_B}{\rho \cdot w}\right) dw = -\frac{F_A - F_B}{\rho \cdot U} \cdot \ln(w) \Big|_{L_0}^{L_0 - tc \cdot U} \tag{38}$$

$$= -\frac{F_A - F_B}{\rho \cdot U} \cdot \begin{cases} \ln\left(\frac{L_0 - U \cdot t}{L_0}\right), & \text{if } t \leq tc \\ \ln\left(\frac{L_0 - U \cdot tc}{L_0}\right), & \text{if } t > tc \end{cases} \tag{39}$$

From equation (39), the integral of $V_B(t)$ for $0 < t < tc$ in equations (33 and 34) is as in equation (40).

$$\frac{Ca \cdot U \cdot t}{2} - \frac{F_A - F_B}{\rho \cdot U} \cdot \ln\left(\frac{L_0 - U \cdot t}{L_0}\right) \tag{40}$$

Combining the result of equation (40) with equations (33, 34, 35) provides equations (41 to 44) used to determine V_B for all conditions tested in the current study, where: tm is the time at which any given contraction event ceases; and Z is a constant required to correct for the assumed linear relationship between median cell stiffness and both F_A and F_B, such that $ZS_A = F_A$, and $ZS_B = F_B$. Maximum pressure drop was calculated from equation (13).

Where $S_A > S_B$, and tm is ≤ tc, V_B is calculated by equation (41).

$$V_B = \frac{Ca \cdot U \cdot tm}{2} - \frac{Z \cdot (S_A - S_B)}{\rho \cdot U} \cdot \ln\left(\frac{L_0 - U \cdot tm}{L_0}\right) \tag{41}$$

Where $S_A > S_B$, and tm is > tc, V_B is calculated by equation (42), noting that tm cannot exceed L_0/U.

$$V_B = \frac{Ca \cdot U \cdot tc}{2} - \frac{Z \cdot (S_A - S_B)}{\rho \cdot U} \cdot \ln\left(\frac{L_0 - U \cdot tc}{L_0}\right) + Ca \cdot U \cdot (tm - tc) \quad (42)$$

Where $S_A < S_B$, and tm is ≤ tc, V_B is calculated by equation (41).
Where $S_A < S_B$, and tm is > tc, V_B is calculated by equation (43).

$$V_B = \frac{Ca \cdot U \cdot tc}{2} - \frac{Z \cdot (S_A - S_B)}{\rho \cdot U} \cdot \ln\left(\frac{L_0 - U \cdot tc}{L_0}\right) \quad (43)$$

Where $S_A = S_B$, V_B is calculated by equation (44).

$$V_B = \frac{Ca \cdot U \cdot tm}{2} \quad (44)$$

Estimation of stiffness correction factor Z. From equation (32), tc becomes negative when $Lo/U < | (2Z(F_A - F_B)/(Ca\rho U^2) |$ to generate meaningless negative values for time. To overcome this difficulty, tc was assigned a value of zero on such occasions during simulations, but since Q_B is maximal at CaU when tc=0 (equations (41, 42, 43), (Fig. 1e), this reduces sensitivity of the system to the effect of $(S_A - S_B)$ in varying transfer. Similarly, if Z is chosen such that $| (2Z(F_A - F_B)/(Ca\rho U^2) |$ approaches L_0/U, Q_B approaches CU/2, which although conservative for estimation of total transfer to Receptor Cells B, also fails to fully test the effect of $(S_A - S_B)$.

Preliminary simulations revealed that letting Z = 1/(median stiffness of all cells A and B considered together) = 6.9726×10^{-5}, generated values for tc that were usually positive, and also provided fair testing of the effect of $(S_A - S_B)$ by often positioning tc in the mid-range between 0 and L_0/U.

Generation of simulated populations of SAOS-2 and fibroblasts. As detailed in the MATLAB R2016a (MathWorks Inc) script provided below, frequency distributions of experimental data were first prepared by binning at convenient values, found to be: 1500 Pa for SAOS-2 stiffness; 3000 Pa for fibroblast stiffness; 6 DiO fluorescence units for SAOS-2 DiO; 1.5 DiD fluorescence units for SAOS-2 DiD; 3 DiD fluorescence units for fibroblast DiD; 0.5 DiO fluorescence units for fibroblast DiO, and 1000μm^2 for area.

An estimated cumulative distribution function (ECDF) was then calculated for each of these variables on basis of the binned input data. Formulae for linear equations connecting midpoints of bins were established, and extrapolated to probability values of 0 and 1 in the first and last bins respectively. Random numbers between 0 and 1 were used to select probability values for substitution into the relevant linear equations describing the smoothed ECDF. Simulated stiffness or fluorescence values were then calculated, with frequency distributions comparable to that of input data. Where input data had values at or approaching zero, it was necessary to remove biologically meaningless values, by firstly determining the minimum input data value, and then substituting all ECDF derived values below this threshold with zero. This approach generated distributions for variables closely approximating those of experimental data. This method was used to generate 5100

donor fibroblasts, 5100 donor SAOS-2, 5000 recipient SAOS-2, and 5000 recipient fibroblasts (Fig. 7).

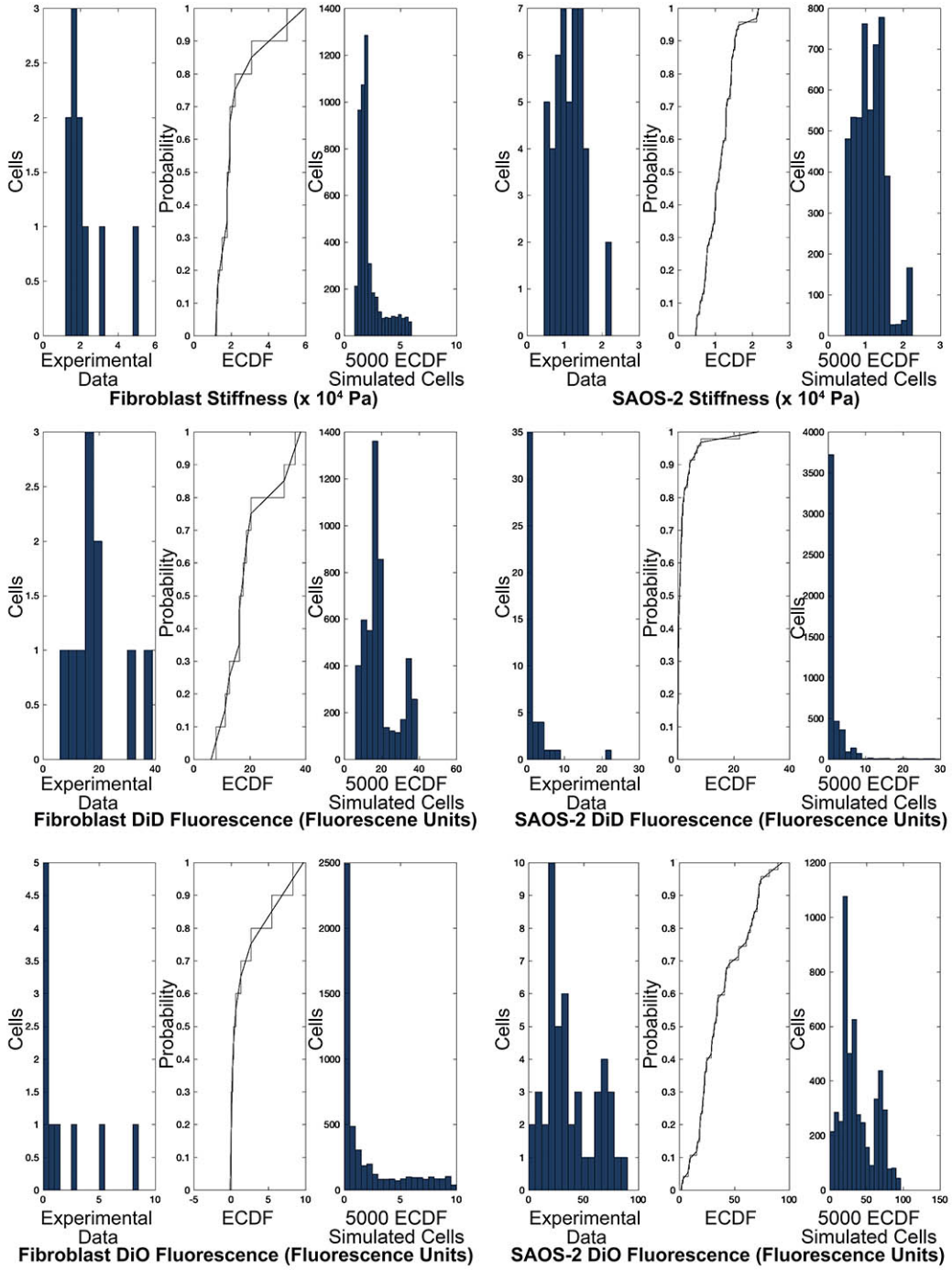

Figure 7. *Histograms for experimental data for stiffness, DiD fluorescence and DiO fluorescence in co-cultured SAOS-2 and fibroblasts, as well as stair plots for the ECDF of these data with superimposed linear smoothing, and histograms for 5000 simulated cells generated by the ECDFs shown. Histograms of simulated cells had distribution profiles very similar to that of experimental data, despite the limited sampling available. Binning for histograms was: 3000 kPa for fibroblast stiffness; 1500 kPa for SAOS-2 stiffness; 3 DiD fluorescence units for fibroblast DiD; 1.5 DiD fluorescence units for SAOS-2 DiD; 0.5 DiO fluorescence units for fibroblast DiO; and 6 DiO fluorescence units for SAOS-2 DiO.*

Simulation of cytoplasmic and fluorescence transfer from one cell population to another.

Definition of variables for calculation. Values for cell stiffness and fluorescence were simulated by ECDF as described above. Separate lists were prepared for values for each of the further variables used in calculations. Values loaded into these lists had distributions bounded by target minimum and maximum values, while target minima and maxima were established at the start of each simulation. Variables modelled in this way were: the number of Donor Cells A each Receptor Cell B could interact with; the number of transfer events each Receptor Cell B could have with each Donor Cell A; the flow rate (U) for each transfer event; the length at time 0 (L_0) of each cell-projection; the radius (r) of each cell-projection; and the viscosity of cytoplasm (η).Values for these parameters, were inferred on basis of confocal microscopy observations, with exception of viscosity, which was taken from the literature [38,40]. Each list held a number of values equivalent to the number of recipient cells modeled, which in the current study was 5000, while random selection was made from these lists for each calculation. The only exception to this approach was for the time permitted for each transfer event, the maximum of which is defined by L_0/U, and random choice of time was made from a pre-determined range between 0 and L_0/U.

Both the number of cells A available for interaction with individual cells B, and the discrete number of exchange events between individual cells A and B, are inherently quantal, so that only zero and positive integers were accepted in lists for these two variables. Other variables were, however, continuous in nature, so that zero and all positive values were accepted.

Cell height and cell profile area values were used to relate calculated volume transfers to fluorescence transfers. Average SAOS-2 and fibroblast cell height was determined from AFM data (3.89×10^{-6}m and 2.36×10^{-6}m respectively), while average SAOS-2 and fibroblast cell surface area ($1.53 \times 10^{-9}m^2$ and $5.34 \times 10^{-9}m^2$ respectively) was established by image analysis from separate experiments.

Calculation of flow volume and fluorescence transfer. In co-cultures, spatial limitations necessarily limit access of any single recipient cell, to only a small group of potential donor cells. Failure to mimic this was found to affect results in preliminary work. For this reason, access of recipient cells to prospective donor cells was limited through a 'sliding window' that widened or closed according to random selection from the relevant variable list, and that shifted to access further donor cells, only after all calculations for any single recipient cell were complete.

Once a cell pairing was established, volume transfer from donor to recipient cell was then calculated by iterative application of equations (32, 41, 42, 43, 44), according to the number of exchanges instructed for that paring as selected at random from the relevant list, while all remaining variables for equations (32, 41, 42, 43, 44) were also selected at random from relevant lists. Volume transfer for the particular cell pairing was then totaled. Total fluorescence transfer for the pairing was further calculated by the product of calculated donor cell fluorescence units per m^3 with volume, and distribution of that fluorescence across the surface area assigned Recipient Cell B. Also recorded were the maximum pressure values attained for each transfer event during flow into both Donor Cells A (P_A) and Recipient Cells B (P_B).

The above procedure was repeated for all simulated Recipient Cells B, to generate result lists of: total Donor Cell A cytoplasmic volume and fluorescence at the level of each recipient cell modeled; and volumes, P_A, P_B and exchange time values for each exchange event modeled. Trial and error was used to identify ranges for

variables that generated results in simulations that were comparable to those determined by experiment. Important considerations selecting conditions for simulation, were that: flow rates, times for individual exchange events, and cell-projection radius and length values be within ranges suggested by time-lapse microscopy; and that calculated pressure values be suitably modest. Histograms of input variables and simulated fluorescence and volume transfer outcomes for the simulations approximating experimental observations (Fig. 6, main manuscript), are shown in Figs. 8 and 9. Data were analyzed using PRISM 7 (GraphPad Software Inc), and Mann Whitney U Tests where appropriate.

Both the number of cells A available for interaction with individual cells B, and the discrete number of exchange events between individual cells A and B, are inherently quantal, so that only zero and positive integers were accepted in lists for these two variables. Other variables were, however, continuous in nature, so that zero and all positive values were accepted.

Cell height and cell profile area values were used to relate calculated volume transfers to fluorescence transfers. Average SAOS-2 and fibroblast cell height was determined from AFM data (3.89×10^{-6}m and 2.36×10^{-6}m respectively), while average SAOS-2 and fibroblast cell surface area ($1.53 \times 10^{-9}m^2$ and $5.34 \times 10^{-9}m^2$ respectively) was established by image analysis from separate experiments.

Calculation of flow volume and fluorescence transfer. In co-cultures, spatial limitations necessarily limit access of any single recipient cell, to only a small group of potential donor cells. Failure to mimic this was found to affect results in preliminary work. For this reason, access of recipient cells to prospective donor cells was limited through a 'sliding window' that widened or closed according to random selection from the relevant variable list, and that shifted to access further donor cells, only after all calculations for any single recipient cell were complete.

Once a cell pairing was established, volume transfer from donor to recipient cell was then calculated by iterative application of equations (32, 41, 42, 43, 44), according to the number of exchanges instructed for that paring as selected at random from the relevant list, while all remaining variables for equations (32, 41, 42, 43, 44) were also selected at random from relevant lists. Volume transfer for the particular cell pairing was then totaled. Total fluorescence transfer for the pairing was further calculated by the product of calculated donor cell fluorescence units per m^3 with volume, and distribution of that fluorescence across the surface area assigned Recipient Cell B. Also recorded were the maximum pressure values attained for each transfer event during flow into both Donor Cells A (P_A) and Recipient Cells B (P_B).

The above procedure was repeated for all simulated Recipient Cells B, to generate result lists of: total Donor Cell A cytoplasmic volume and fluorescence at the level of each recipient cell modeled; and volumes, P_A, P_B and exchange time values for each exchange event modeled. Trial and error was used to identify ranges for variables that generated results in simulations that were comparable to those determined by experiment. Important considerations selecting conditions for simulation, were that: flow rates, times for individual exchange events, and cell-projection radius and length values be within ranges suggested by time-lapse microscopy; and that calculated pressure values be suitably modest. Histograms of input variables and simulated fluorescence and volume transfer outcomes for the simulations approximating experimental observations (Fig. 6), are shown in Figs. 8 and 9. Data were analyzed using PRISM 7 (GraphPad Software Inc), and Mann Whitney U Tests where appropriate.

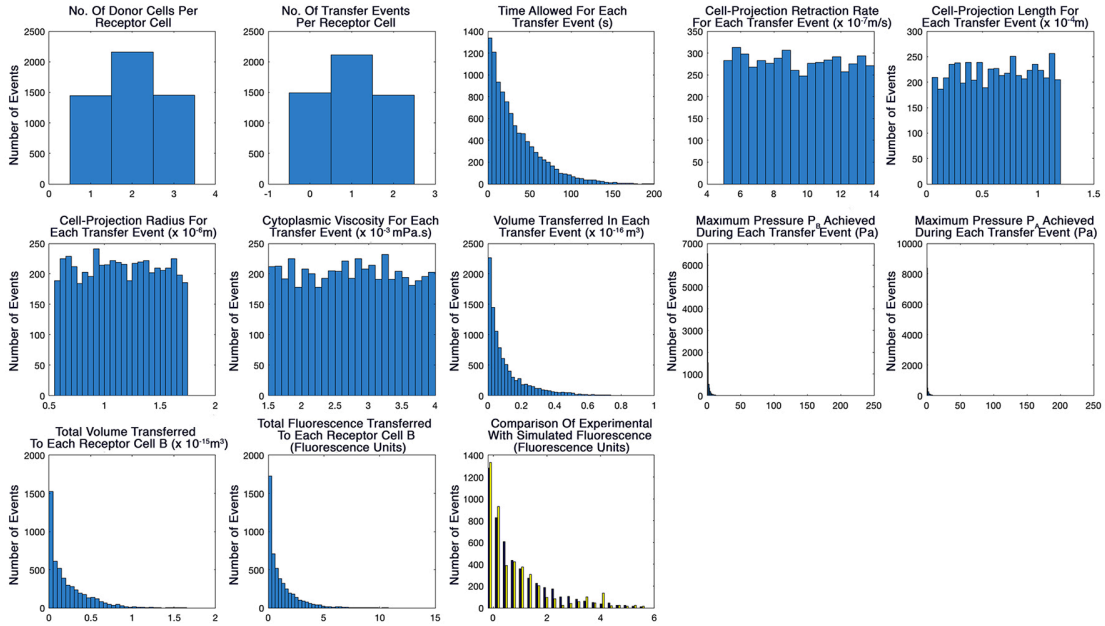

Figure 8. *Histogram output of MATLAB script for simulation of CPP transfer from fibroblasts to SAOS-2 comparable to that seen by experiment, and shown in Fig. 6 and Tables 1 and 2 of the main manuscript. Modest central tendency was seen for the number of donor cells receptor cells interacted with, as well as for the number of transfer events per receptor cell. Input variables for cell-projection retraction rate, length, radius and viscosity had essentially uniform distributions, while time permitted for transfer events was within range of time-lapse observations. Pressures generated during transfer were modest with exception of only a few simulated values (median maximal Pressure B was 0.668 Pa, 2.91% over 10 Pa), while volume and fluorescence transfer was appreciable, closely approximating experimental fluorescence data.*

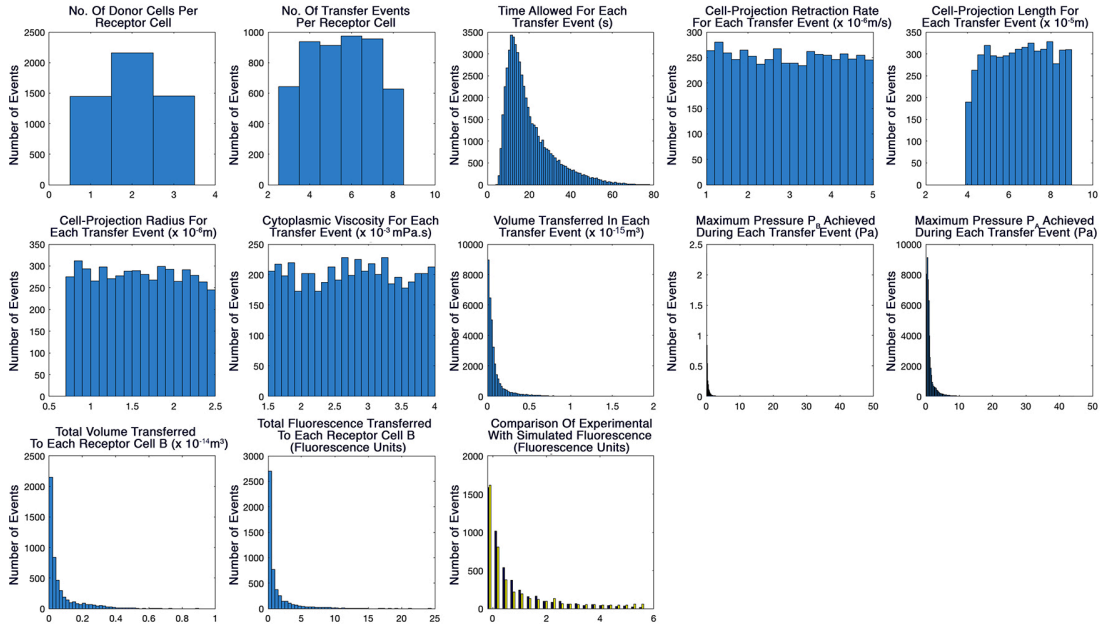

Figure 9. *Histogram output of MATLAB script for simulation of CPP transfer from SAOS-2 to fibroblasts comparable to that seen by experiment, and shown in Fig. 6 and Tables 1 and 2 of the main manuscript. Modest central tendency was seen for the number of donor cells receptor cells interacted with, as well as for the number of transfer events per receptor cell. Input variables for cell-projection retraction rate, length, radius and viscosity had essentially flat distributions, while time permitted for transfer events was within range of time-lapse observations. Pressures generated during transfer were modest with exception of only a few simulated values (median maximal Pressure B was 0.144 Pa, 0.40% over 10 Pa), while volume and fluorescence transfer was appreciable, closely approximating experimental fluorescence data.*

Acknowledgements
We thank the Memorial Sloan Kettering Cancer Center, including via MSKCC P30 CA008748 Cancer Center Support Grant, as well as the Australian Dental Research Fund for their support of this work. We also thank an anonymous donor for their generous contribution. In addition, we thank Dr R Norden of the Graduate School of Biomedical Engineering, The University of NSW, for his advice.

Supplementary Information
Supplementary information includes: Supplementary figures supporting that exchange of fluorescent label was inconsistent with: non-specific label transfer, TNT, phagocytosis of cell fragments, or exosomes or other micro-vesicles; MATLAB script used for generation of ECDF and simulated fluorescence transfer; and supplementary movies.

Author Contributions
HZ conceived, designed and conducted all experiments, mathematical and numerical modelling, and also prepared the manuscript. EK assisted with cell culture. NP and KM assisted with AFM coupled with fluorescence imaging, while YR, VB, SF and KM assisted with CLSM and quantitation of fluorescence. GR and JC provided valuable input for mathematical and numerical modelling respectively, while GWL assisted in preparation of movies. All authors including BC and MASM contributed to critical analysis and preparation of the manuscript.

References
1 David, M. S. *et al.* Membrane and cytoplasmic marker exchange between malignant neoplastic cells and fibroblasts via intermittent contact: increased tumour cell diversity independent of genetic change. *J Pathol* **228**, 495-505, doi:10.1002/path.4063 (2012).

2 Sinclair, K. A., Yerkovich, S. T., Hopkins, P. M. & Chambers, D. C. Characterization of intercellular communication and mitochondrial donation by mesenchymal stromal cells derived from the human lung. *Stem Cell Res Ther* **7**, 91, doi:10.1186/s13287-016-0354-8 (2016).

3 Lehmann, T. P. *et al.* Coculture of human nucleus pulposus cells with multipotent mesenchymal stromal cells from human bone marrow reveals formation of tunnelling nanotubes. *Mol Med Rep* **9**, 574-582, doi:10.3892/mmr.2013.1821 (2014).

4 Lehmann, T. P. *et al.* Quantification of the asymmetric migration of the lipophilic dyes, DiO and DiD, in homotypic co-cultures of chondrosarcoma SW-1353 cells. *Mol Med Rep* **14**, 4529-4536, doi:10.3892/mmr.2016.5793 (2016).

5 Pasquier, J. *et al.* Preferential transfer of mitochondria from endothelial to cancer cells through tunneling nanotubes modulates chemoresistance. *Journal of translational medicine* **11**, 94, doi:10.1186/1479-5876-11-94 (2013).

6 Islam, M. N. *et al.* Mitochondrial transfer from bone-marrow-derived stromal cells to pulmonary alveoli protects against acute lung injury. *Nat Med* **18**, 759-765, doi:10.1038/nm.2736 (2012).

7 Liu, K. *et al.* Mesenchymal stem cells rescue injured endothelial cells in an in vitro ischemia-reperfusion model via tunneling nanotube like structure-mediated mitochondrial transfer. *Microvasc Res* **92**, 10-18, doi:10.1016/j.mvr.2014.01.008 (2014).

8 Spees, J. L., Olson, S. D., Whitney, M. J. & Prockop, D. J. Mitochondrial transfer between cells can rescue aerobic respiration. *Proc Natl Acad Sci U S A* **103**, 1283-1288, doi:10.1073/pnas.0510511103 (2006).
9 Vallabhaneni, K. C., Haller, H. & Dumler, I. Vascular smooth muscle cells initiate proliferation of mesenchymal stem cells by mitochondrial transfer via tunneling nanotubes. *Stem Cells Dev* **21**, 3104-3113, doi:10.1089/scd.2011.0691 (2012).
10 Koyanagi, M., Brandes, R. P., Haendeler, J., Zeiher, A. M. & Dimmeler, S. Cell-to-cell connection of endothelial progenitor cells with cardiac myocytes by nanotubes: a novel mechanism for cell fate changes? *Circulation research* **96**, 1039-1041, doi:01.RES.0000168650.23479.0c [pii] 10.1161/01.RES.0000168650.23479.0c (2005).
11 Davis, D. M. & Sowinski, S. Membrane nanotubes: dynamic long-distance connections between animal cells. *Nat Rev Mol Cell Biol* **9**, 431-436, doi:10.1038/nrm2399 (2008).
12 Gerdes, H. H., Rustom, A. & Wang, X. Tunneling nanotubes, an emerging intercellular communication route in development. *Mech Dev* **130**, 381-387, doi:10.1016/j.mod.2012.11.006 (2013).
13 Onfelt, B. *et al.* Structurally distinct membrane nanotubes between human macrophages support long-distance vesicular traffic or surfing of bacteria. *J Immunol* **177**, 8476-8483 (2006).
14 David, M. S. *et al.* SAOS-2 osteosarcoma cells bind fibroblasts via ICAM-1 and this is increased by tumour necrosis factor-alpha. *PLoS One* **9**, e101202, doi:10.1371/journal.pone.0101202 (2014).
15 David, M. S., Kelly, E. & Zoellner, H. Opposite cytokine synthesis by fibroblasts in contact co-culture with osteosarcoma cells compared with transwell co-cultures. *Cytokine* **62**, 48-51, doi:10.1016/j.cyto.2013.02.028 (2013).
16 Bloemendal, S. & Kuck, U. Cell-to-cell communication in plants, animals, and fungi: a comparative review. *Die Naturwissenschaften* **100**, 3-19, doi:10.1007/s00114-012-0988-z (2013).
17 Caneparo, L., Pantazis, P., Dempsey, W. & Fraser, S. E. Intercellular bridges in vertebrate gastrulation. *PLoS One* **6**, e20230, doi:10.1371/journal.pone.0020230 (2011).
18 Herst, P. M., Dawson, R. H. & Berridge, M. V. Intercellular communication in tumour biology: A role for mitochondrial transfer. *Frontiers in oncology* **8**, 344-353, doi:10.3389/fonc.2018.00344 (2018).
19 Ahmed, K. A. & Xiang, J. Mechanisms of cellular communication through intercellular protein transfer. *J Cell Mol Med* **15**, 1458-1473, doi:JCMM1008 [pii] 10.1111/j.1582-4934.2010.01008.x (2011).
20 Ady, J. W. *et al.* Intercellular communication in malignant pleural mesothelioma: properties of tunneling nanotubes. *Frontiers in physiology* **5**, 400, doi:10.3389/fphys.2014.00400 (2014).
21 Lou, E. *et al.* Tunneling Nanotubes: A new paradigm for studying intercellular communication and therapeutics in cancer. *Communicative & integrative biology* **5**, 399-403, doi:10.4161/cib.20569 (2012).
22 Lou, E. *et al.* Tunneling nanotubes provide a unique conduit for intercellular transfer of cellular contents in human malignant pleural mesothelioma. *PLoS One* **7**, e33093, doi:10.1371/journal.pone.0033093 (2012).
23 Ariazi, J. *et al.* Tunneling Nanotubes and Gap Junctions-Their Role in Long-Range Intercellular Communication during Development, Health, and Disease Conditions. *Front Mol Neurosci* **10**, 333, doi:10.3389/fnmol.2017.00333 (2017).
24 Delage, E. *et al.* Differential identity of Filopodia and Tunneling Nanotubes revealed by the opposite functions of actin regulatory complexes. *Scientific reports* **6**, 39632, doi:10.1038/srep39632 (2016).

25 Thayanithy, V. *et al.* Tumor exosomes induce tunneling nanotubes in lipid raft-enriched regions of human mesothelioma cells. *Exp Cell Res* **323**, 178-188, doi:10.1016/j.yexcr.2014.01.014 (2014).
26 Zoellner, H., Paknejad, N., Manova, K. & Moore, M. A. A novel cell-stiffness-fingerprinting analysis by scanning atomic force microscopy: comparison of fibroblasts and diverse cancer cell lines. *Histochem Cell Biol* **144**, 533-542, doi:10.1007/s00418-015-1363-x (2015).
27 Manoussaki, D., Shin, W. D., Waterman, C. M. & Chadwick, R. S. Cytosolic pressure provides a propulsive force comparable to actin polymerization during lamellipod protrusion. *Scientific reports* **5**, 12314, doi:10.1038/srep12314 (2015).
28 Charras, G. T., Yarrow, J. C., Horton, M. A., Mahadevan, L. & Mitchison, T. J. Non-equilibration of hydrostatic pressure in blebbing cells. *Nature* **435**, 365-369, doi:10.1038/nature03550 (2005).
29 Strychalski, W. & Guy, R. D. Intracellular Pressure Dynamics in Blebbing Cells. *Biophys J* **110**, 1168-1179, doi:10.1016/j.bpj.2016.01.012 (2016).
30 Petrie, R. J., Gavara, N., Chadwick, R. S. & Yamada, K. M. Nonpolarized signaling reveals two distinct modes of 3D cell migration. *J Cell Biol* **197**, 439-455, doi:10.1083/jcb.201201124 (2012).
31 Law, J. & Rennie, R. in *A dictionary of physics* (eds J. Law & R. Rennie) (Oxford University Press, Oxford, 2009).
32 Darby, R. & Chhabra, R. P. *Chemical engineering fluid mechanics*. 3 edn, (CRC Press, 2016).
33 Fairchild, C. L. & Barna, M. Specialized filopodia: at the 'tip' of morphogen transport and vertebrate tissue patterning. *Curr Opin Genet Dev* **27**, 67-73, doi:10.1016/j.gde.2014.03.013 (2014).
34 Scott, G., Leopardi, S., Printup, S. & Madden, B. C. Filopodia are conduits for melanosome transfer to keratinocytes. *J Cell Sci* **115**, 1441-1451 (2002).
35 Singh, S. K. *et al.* Melanin transfer in human skin cells is mediated by filopodia--a model for homotypic and heterotypic lysosome-related organelle transfer. *FASEB J* **24**, 3756-3769, doi:10.1096/fj.10-159046 (2010).
36 Ma, H. J. *et al.* alpha-Melanocyte stimulating hormone (MSH) and prostaglandin E2 (PGE2) drive melanosome transfer by promoting filopodia delivery and shedding spheroid granules: Evidences from atomic force microscopy observation. *J Dermatol Sci* **76**, 222-230, doi:10.1016/j.jdermsci.2014.09.005 (2014).
37 LeBleu, V. S. & Kalluri, R. A peek into cancer-associated fibroblasts: origins, functions and translational impact. *Dis Model Mech* **11**, doi:10.1242/dmm.029447 (2018).
38 Fushimi, K. & Verkman, A. S. Low viscosity in the aqueous domain of cell cytoplasm measured by picosecond polarization microfluorimetry. *J Cell Biol* **112**, 719-725 (1991).
39 Plaza, G. R. *et al.* Simple measurement of the apparent viscosity of a cell from only one picture: Application to cardiac stem cells. *Phys Rev E Stat Nonlin Soft Matter Phys* **90**, 052715, doi:10.1103/PhysRevE.90.052715 (2014).
40 Kalwarczyk, T. *et al.* Comparative analysis of viscosity of complex liquids and cytoplasm of mammalian cells at the nanoscale. *Nano letters* **11**, 2157-2163, doi:10.1021/nl2008218 (2011).
41 Barthel, E. Adhesive elastic contacts - JKR and more. *Journal of Physics D: Applied Physics* **41**, 163001-163041, doi:doi:10.1088/0022-3727/41/16/163001 (2008).
42 Cross, S. E. *et al.* AFM-based analysis of human metastatic cancer cells. *Nanotechnology* **19**, 384003, doi:10.1088/0957-4484/19/38/384003 (2008).

43 Watanabe, T. *et al.* Epithelial-mesenchymal transition in human gastric cancer cell lines induced by TNF-alpha-inducing protein of Helicobacter pylori. *Int J Cancer* **134**, 2373-2382, doi:10.1002/ijc.28582 (2014).
44 Weder, G. *et al.* Increased plasticity of the stiffness of melanoma cells correlates with their acquisition of metastatic properties. *Nanomedicine : nanotechnology, biology, and medicine* **10**, 141-148, doi:10.1016/j.nano.2013.07.007 (2014).
45 Akhremitchev, B. B. & Walker, G. C. Finite sample thickness effects on elasticity determination using atomic force microscopy. *Langmuir* **15**, 5630-5634, doi:Doi 10.1021/La980585z (1999).
46 Costa, K. D. & Yin, F. C. P. Analysis of indentation: Implications for measuring mechanical properties with atomic force microscopy. *J Biomech Eng-T Asme* **121**, 462-471, doi:Doi 10.1115/1.2835074 (1999).
47 Bello, D. J. & Lecki, F. A. *Strength and stiffness of engineering systems*. (Springer, 2009).